# Middle Ear Pressure Gain and Cochlear Input Impedance in the Chinchilla

By

Michaël C. C. Slama

Diplôme d'Etudes Musicales, Conservatoire National de Région de Metz, 2004
Ingénieur, Ecole Supérieure d'Electricité, 2004
M.S., Electrical and Computer Engineering, Georgia Institute of Technology, 2005

SUBMITTED TO THE DEPARTMENT OF ELECTRICAL ENGINEERING AND
COMPUTER SCIENCE IN PARTIAL FULFILLMENT OF THE REQUIREMENTS
FOR THE DEGREE OF

MASTER OF SCIENCE IN ELECTRICAL ENGINEERING
AND COMPUTER SCIENCE AT THE
MASSACHUSETTS INSTITUTE OF TECHNOLOGY

JUNE 2008

Signature of Author:_____
Michaël C. C. Slama
Harvard-MIT Division of Health Sciences & Technology
May 22, 2008

Certified by:_____
John J. Rosowski
Professor of Otology & Laryngology and Health Sciences & Technology
Harvard Medical School and Harvard-MIT Division of Health Sciences & Technology
Thesis Supervisor

Accepted by:_____
Terry P. Orlando
Professor of Electrical Engineering
Chair, Department Committee on Graduate Students

# Middle Ear Pressure Gain and Cochlear Input Impedance in the Chinchilla

By

Michaël C. C. Slama

Submitted to the Department of Electrical Engineering and Computer Science
on May 22, 2008 in Partial Fulfillment of the Requirements for the Degree of
Master of Science in Electrical Engineering and Computer Science

## Abstract

Measurements of middle ear conducted sound pressure in the cochlear vestibule $P_V$ have been performed in only a few individuals from a few mammalian species. Simultaneous measurements of sound-induced stapes velocity $V_S$ are even more rare. We report simultaneous measurements of $V_S$ and $P_V$ in chinchillas. The $V_S$ measurements were performed using single-beam laser-Doppler vibrometry; $P_V$ was measured with fiber-optic pressure sensors like those described by Olson [JASA 1998; 103: 3445-63]. Accurate in-vivo measurements of $P_V$ are limited by anatomical access to the vestibule, the relative sizes of the sensor and vestibule, and damage to the cochlea when inserting the measurement device. The small size (170 µm diameter) of the fiber-optic pressure sensors helps overcome these three constraints.

$P_V$ and $V_S$ were measured in six animals, and the middle ear pressure gain (ratio of $P_V$ to the sound pressure in the ear canal) and the cochlear input impedance (ratio of $P_V$ to the product of $V_S$ and area of the footplate) computed. Our measurements of middle ear pressure gain are similar to published data in the chinchilla at stimulus frequencies of 500 Hz to 3 kHz, but are different at other frequencies. Our measurements of cochlear input impedance differ somewhat from previous estimates in the chinchilla and show a resistive input impedance up to at least 10 kHz. To our knowledge, these are the first direct measurements of this impedance in the chinchilla. The acoustic power entering the cochlea was computed based on our measurements of input impedance. This quantity was a good predictor for the audiogram at frequencies below 1 kHz.

Thesis Supervisor: John J. Rosowski
Title: Professor of Otology & Laryngology and Health Sciences & Technology, Harvard Medical School and Harvard-MIT Division of Health Sciences & Technology

# Acknowledgements

# Table of Contents

# 1. Introduction

The peripheral auditory system transmits sound from the outside world (speech, music, environment, noise…) to the central auditory system. This process is very complex and can be decomposed into several stages, related to the subdivisions of the auditory periphery (Figure 1.1). The outer ear, consisting of the pinna, the concha, the external auditory canal and the lateral surface of the tympanic membrane (TM), collects sound and directs it towards the middle ear, which in turns transmits the TM vibrations toward the inner ear. These vibrations are sensed by the hair cells of the cochlea, and transduced into neural impulses that are transmitted to the central auditory system via the auditory nerve.

In this section, we will focus more particularly on the anatomy of the middle ear, and on ways to model its components. We will then briefly describe what is known of middle ear function, before introducing the specific goals and hypotheses that we examined in this study.

## 1.1 Anatomy of the Middle Ear

Figure 1.2 shows a simplified representation of the peripheral auditory system of a terrestrial mammal (Rosowski, 1991). The main components of the middle ear are the medial surface of the tympanic membrane (TM), the ossicular chain, the eustachian tube and the middle ear muscles.

The TM acts as a pressure sensitive membrane and is mechanically coupled to the ossicular chain. Birds and reptiles only have one ossicle whereas in mammals, the ossicular chain is made of 3 ossicles (the hammer-shaped malleus, the anvil-shaped incus, and the stirrup-shaped stapes). The manubrium (handle) of the malleus is attached to the TM by connective tissue. The 3 ossicles are connected by 2 joints: the incudo-mallear joint (between the head of the malleus and the body of the incus), and the incudo-stapedial joint (between the lenticular process of the incus and the head of the stapes). To a first approximation, malleus and incus move in a rotational way, whereas stapes motion is piston-like.

The eustachian tube connects the middle ear air space to the naso-pharynx, and helps keep the middle ear static pressure close to atmospheric pressure by opening periodically during swallowing and yawning.

The middle ear muscles are the tensor tympani (attached to the manubrium of the malleus) and the stapedius (attached to the head of the stapes). These muscles contract in response to loud sounds or during speech production to change the response of the middle ear and attenuate the incoming sound (Borg and Zakrisson, 1973). This protective function is called the middle ear reflex.

In some mammals, including the chinchilla, the tympanic cavity is extended by a thin-walled bony capsule called the "bulla".

## 1.2 Modeling the Middle Ear

The input to the middle ear is the pressure in the ear canal, near the TM, $P_{TM}$, which is associated with the TM volume velocity $U_{TM}$. These acoustic variables are converted into mechanical variables at the TM (Rosowski, 1994). If we consider the TM as a piston of area $A_{TM}$, then $P_{TM}$ is converted into the force $F_M = P_{TM} \times A_{TM}$ acting on the malleus, and $U_{TM}$ becomes the linear velocity $V_{TM} = \dfrac{U_{TM}}{A_{TM}}$. $F_M$, $V_{TM}$ and the load to the middle ear $Z_C$, produce a force $F_S$ and a velocity $V_S$ at the stapes. The stapes footplate acts on the fluid-filled vestibule (entrance of the cochlea) as a piston of area $A_{FP}$, at least to a first approximation, resulting in a pressure in the vestibule of the inner ear $P_V = \dfrac{F_S}{A_{FP}}$ and a volume velocity of the stapes $U_S = V_S \times A_{FP}$. The vestibule pressure created by stapes motion produces a rapid wave of sound in the cochlear fluid that propagates through the inner ear to set the round window of the inner ear in motion. This "fast-wave" pressure produces a pressure-difference across the cochlear partition that excites the much slower cochlear traveling wave that causes the basilar membrane to vibrate. Hair cells amplify and transduce basilar-membrane motion into neural spikes that are transmitted to the central auditory system.

Given the small ratio between the size of the anatomical structures and the wavelength of sound at frequencies within the hearing range, lumped-element

approximation can usually be used to model the outer and middle ears. In this framework, there is a simple relationship between an across variable (*P*, the pressure across the element, or *F*, the mechanical force acting on the element), and a through variable (respectively *U*, the volume velocity through the element, and *V*, the linear velocity of the element). There are 4 types of lumped-elements (Beranek, 1996): resistances, masses, compliances (or their inverse: stiffnesses) and transformers. Figure 1.3 shows a model of the middle ear in the cat (Puria and Allen, 1998) that accounts for the masses of the middle ear ossicles and the stiffness and damping within the supporting and connecting ligaments.

## 1.3  Notion of Impedance

The ratio of an across variable to a through variable is called impedance. We can define an electrical impedance as the ratio of voltage to current, a mechanical impedance as the ratio of force to velocity, and an acoustic impedance as the ratio of pressure to volume velocity. Resistances, masses and compliances are simple examples of impedances.

For a resistance, across and through variables are linearly related: $P = R_A \times U$ or $F = R_M \times V$. An acoustic resistance will typically be a very narrow tube. In that case, $R_A = \frac{8 \eta l}{\pi a^4}$ with $\eta$ the viscosity of the fluid, *l* the length of the tube, and *a* the radius of the tube (Beranek, 1996). A tube of moderate cross-section but infinite length can also be modeled as a resistance with $R_A = \frac{\rho c}{\pi a^2}$ with $\rho$ the density of the fluid and *c* the speed of sound. The unit of acoustic resistance is the Acoustic Ohm (Pa-s/m$^3$).

In the case of a mass, $P = j \omega M_A \times U$ and $F = j \omega M_M \times V$. An open-ended cylindrical tube will typically behave as an acoustic mass defined by the length *l* and radius *a* of the tube and the density $\rho$ of the air within the tube, $M_A = \frac{\rho l}{\pi a^2}$. The acoustic mass can also be seen as the actual mass of fluid in the tube divided by the square of the cross-section area, and has units of kg/m$^4$.

Finally, in the case of a compliance, $P = \dfrac{1}{j\omega C_A} \times U$ and $F = \dfrac{1}{j\omega C_M} \times V$. A typical acoustic compliance will be a small enclosed volume of air. In that case, $C_A = \dfrac{Volume}{AdiabaticBulkModulus} = \dfrac{V}{\rho c^2}$, where $c$ is the propagation velocity of sound in air. The unit of acoustic compliance is $m^3/Pa$.

Many systems can be described by series or parallel combinations of these basic impedances.

## 1.4 Middle Ear Function

von Helmoltz (1877) first described the middle ear as a system that improved the coupling between sound power in air and sound power in liquid by matching the impedances of these two media. He modeled the middle ear as an ideal transformer composed of several levers in cascade. First, the difference between the area of the TM and the area of the stapes footplate has the effect of a pneumatic lever with ratio $\dfrac{A_{TM}}{A_{FP}}$.

Moreover, the rotational motion of the malleus and incus, associated with the difference in their lengths, creates an ossicular lever with ratio $\dfrac{l_M}{l_I}$. According to this model, the total transformer ratio is therefore: $\dfrac{P_V}{P_{TM}} = \dfrac{U_{TM}}{U_S} = \dfrac{A_{TM}}{A_{FP}} \times \dfrac{l_M}{l_I}$

In terrestrial mammals, $\dfrac{A_{TM}}{A_{FP}}$ ranges between 10 and 40 (Rosowski, 1996), whereas the ossicular ratio is a lot smaller (about 1.2 in humans). In the chinchilla, the area ratio is about 28 (Vrettakos *et al.*, 1988) and the ossicular ratio is about 2 (Fleischer, 1973). The ratio of areas is therefore the main contribution to the transformer ratio.

The middle ear only acts as an "ideal transformer" (defined by the above equation) if its stiffness, mass and damping are small compared to the impedance that loads the transformer, According to the ideal transformer model, the middle ear pressure gain (the ratio of $P_V$ to $P_{TM}$) should be real and independent of frequency. Previous measurements in chinchilla (Décory, 1989), cat (Nedzelnitsky, 1980) and guinea pig (Dancer and

Franke, 1980), show a complex middle ear gain (Figure 1.4) that depends on frequency; the ideal transformer hypothesis is therefore only a rough approximation.

## 1.5 Aims of this Study

The general goal of this project is to investigate middle ear function in an animal model with a hearing range close to the human range: the chinchilla. Better understanding middle ear function is important to both improve our scientific knowledge of the auditory system and develop therapeutic approaches to diseases and malfunctions of the middle ear. This study has three main aims:

(1) Measure the sound pressure in the vestibule ($P_V$) in living animals in response to acoustic stimulation, in order to <u>quantify the middle ear gain</u> ($G_{ME}$: ratio between the sound pressure at the input of the inner ear $P_V$ and the sound pressure in the ear canal near the TM $P_{TM}$). The measurements will be performed with custom-built fiber-optic miniature pressure sensors (Olson, 1998). The transfer function $P_V/P_{TM}$ depends on frequency and quantifies the passive pressure amplification function of the middle ear. We will compare our measurements with other measurements of $G_{ME}$ in chinchilla and other species.

(2) Simultaneously measure $P_V$ and the sound-induced stapes volume velocity ($U_S$) to <u>quantify the input impedance of the inner ear</u> ($Z_C = P_V / U_S$), which is the load to the middle ear. To our knowledge, these are the first direct measurements of this impedance in the chinchilla. We will compare our measured $Z_C$ with estimates of this quantity in the chinchilla as well as measurements in other species. We will also use our measurements to infer the sound-power delivered to the cochlea for a given ear-canal sound pressure. Of theoretical interest is whether the power output from the middle ear is related to auditory thresholds.

(3) Assess the influence of the hole made in the inner ear to introduce the miniature microphone on the measured sound pressure, so as to <u>estimate the bias introduced by our experimental approach</u>. This assessment will be done both theoretically and experimentally. On the theoretical side, we will use a lumped-element model of the middle and inner ears, in which an impedance representing the hole is added. On the experimental side, we will compare measurements of $U_S$ and $P_V$

with a hole in the vestibule and the pressure microphone in place, with measurements in an intact vestibule or after the hole has been sealed.

# 2. Materials and Methods

## 2.1 Fiber-Optic Pressure Sensors

### 2.1.1 Why fiber-optic pressure sensors?

Measurements of $P_V$ are constrained by the limited space available for the pressure sensors (the volume of the chinchilla vestibule is on the order of 0.5 mm$^3$) and the fragility of the middle ear structures. We chose to use fiber-optic pressure sensors because they have good sensitivity, good high frequency response (up to about 100 kHz), and because they are very small. Their small size (about 170 μm in diameter) insures:

- Minimal disruption of the pressure field in the inner ear at frequencies in the chinchilla's hearing range, both because of the small size (170 μm is less than 1% of the wavelength in water at 30 kHz) and the relatively high impedance associated with such a small microphone: The volume displacement of the diaphragm produced by loud sounds (< 0.4 nL) is less than 0.1% of the fluid volume in the vestibule.

- Minimal damage to the middle ear and inner ear structures during insertion into the vestibule.

### 2.1.2 The optic lever principle

The underlying principle of fiber-optic pressure sensors is the optic-lever principle (Cook and Hamm, 1979). When light is sent through an optical fiber, it exits the fiber with an angle. In an optic lever, a reflecting surface is placed at some distance from the fiber output. In single-fiber models, the exiting cone of light is reflected at the reflecting surface, such that a portion of the exiting light reenters the fiber (Figure 2.1).

The proportion of reentering light depends on the distance between the reflecting surface and the fiber's end (Figure 2.2). When the distance is reduced to 0, the reflecting surface is essentially closing the optic fiber and therefore all the emitted light reenters the fiber. At the other extreme, when the reflecting surface is infinitely far from the fiber end, the proportion of reentering light goes to 0. In between, the power reentering the fiber

follows a law in $\dfrac{1}{d^2}$ with $d$ the distance between the reflecting surface and the fiber. More precisely:

$$W_{in} = W_{out} \frac{1}{\left(1 + 2\tan(\phi)\dfrac{d}{a}\right)^2}$$

with: $a$ as the diameter of the fiber, $\Phi$ the angle of the light exiting the fiber, $W_{out}$ the exiting power, and $W_{in}$ the reentering power (after Cook and Hamm, 1979).

We performed a simple experiment to test this relationship. Light was sent into a fiber using a Light Emitting Diode (LED) and a small mirror was positioned with a micromanipulator at a controlled distance from the end of the fiber. The reflected light reentering the fiber was converted to a DC voltage using a photodiode, and the voltage was monitored with a voltmeter while varying the distance to the mirror. The lower panel of figure 2.2 shows the results obtained. The curve is consistent with the equation above, attaining a maximum for a distance of 0, and decaying asymptotically.

Instead of a rigid reflecting surface, one can use a pressure sensitive reflecting membrane. In a pressure field, the vibrations of the membrane will modulate the distance of the membrane to the end of the fiber, and will therefore modulate the power of the light reentering the fiber, according to the equation above and to figure 2.2. In short, a sound pressure signal can be converted into a light signal thanks to the optic lever system. As the slope of the power vs. distance function is steepest for small distances, we are interested in placing the membrane as close as possible to the end of the fiber, in order to maximize the sensitivity: Small vibration amplitudes Δx will result in large changes in power ΔW (cf. illustration on Figure 2.2 top panel).

### 2.1.3  Design

The fiber-optic pressure sensors were fabricated following the techniques of Olson (1998). For our project, we learned to make and calibrate these microphones. They are composed of a glass capillary tube (167 μm outer diameter) with a gold-coated polymer diaphragm affixed to one end. A single optical fiber (100 μm o.d.) is inserted into the other end (Figure 2.3). The optical fiber is spliced to a "Y" coupling. A light Emitting Diode (LED) attached to one coupler branch produces incoherent light, and a photodiode

attached to the other branch measures the light reflected from the diaphragm. Sound pressure flexes the diaphragm and modulates the reflected light.

### 2.1.4 Manufacturing

The manufacturing process can be broken down into several steps. Some steps were done in our lab, but some others required special equipment and were performed at the Microsystems Technology Laboratories (MTL) at MIT.

#### 2.1.4.1 The optical fiber

The glass tube we used had an inner diameter of about 100 μm, but we could not identify an optical fiber with a matching outer diameter. Therefore, we used slightly bigger fibers, which we etched down to the desired diameter with hydro-fluoric acid (HF). HF has the ability to dissolve $SiO_2$, which is the main component of glass, but it is a very corrosive and toxic acid, with the ability to penetrate quickly biological tissues. Moreover, the symptoms of exposure to HF usually occur some time after exposure. Consequently, HF can only be handled safely in specialized laboratories. We used the MTL, where we wore several layers of protective equipment (coats, gloves, sleeves, goggles, aprons and face-shields) and worked under a hood.

To connect the etched fiber to the "Y" coupler, we used a special fiber fuser. Prior to the fusion splicing process, the ends to be fused had to be stripped, cleaned, and cleaved very precisely, in order to make the facing fiber surfaces perfectly parallel, to avoid any loss of light at the fused junction.

#### 2.1.4.2 Gold-coated diaphragms

The pressure sensitive polymer diaphragms were made of monolayers of UV cured optical adhesive (Norland). A small tub was filled with deionized water, and a drop of adhesive placed on the surface. The drop spreads on the surface, resulting in a thin film, and producing interference patterns in the visible light reflected from the surface of the drop. The number of visible rings decreases as the film becomes thinner. When just a few rings remain, a UV light positioned above the tub is turned on to cure the adhesive. The film of cured adhesive is affixed around the open end of a 1 to 2 cm length of 100 micron i.d. glass capillary tube.

At this stage, the diaphragm made of the cured adhesive is transparent and does not reflect light. To make it reflective, we coat the outer surface of the diaphragm with a thin (about 60 nm) layer of gold. This step was also performed in the MTL where we used an electron-beam evaporator: A vacuum is created in a deposition chamber, and a piece of gold is heated locally by a beam of electrons; the gold evaporates and is deposited onto the diaphragm placed within the chamber.

To be useful, a sensor needs to be sensitive, stable in water, and stable at body temperature. For a typical batch of about 30 coated diaphragms, only 10 to 15 manufactured sensors would show some sensitivity to nearby hand claps in air. Among those, about half would stay sensitive after immersing them in water. Among those remaining, just a couple were not significantly sensitive to temperature. The rate of success for these sensors is therefore very low (2 to 3 out of 30), but a good and stable sensor can be used for several months.

### 2.1.5  Calibration

Calibration of the sensors is done in water, according to the method described by Schloss and Strasberg (1962): the sensor is immersed in a column of liquid that is shaken vertically (Figure 2.4); the pressure at the diaphragm is related to the depth of immersion $h$ and to the acceleration of the shaker $a_x$ by the formula:

$$p_h \cong \rho h a_x$$

The main issues with these sensors are their fragility and their stability. During manipulation or insertion into the vestibule, it was not uncommon to touch a structure with the diaphragm, and change the sensors sensitivity or stability. Temperature also was an issue in some cases. Consequently, we calibrated the sensors repeatedly during an experiment, in order to make sure that the sensitivity of the sensor did not change significantly. We report data only in cases where the sensor's calibration was stable throughout the measurement session.

A typical calibration curve is plotted in Figure 2.5. For this sensor (#44), the magnitude was essentially flat up to 10 kHz, with a value of about 500 Pa/V, and then decreased between 10 and 30 kHz. The angle was roughly flat and close to 0 on the entire range of measurements.

## 2.2 Laser Doppler Vibrometry

To measure stapes velocity, we used a single-beam laser Doppler vibrometer (Polytec CLV 700) aimed at small (< 50 μm diameter) reflective plastic beads placed on the posterior crus and the footplate. Sound-induced velocity of the stapes was measured using the Doppler shift of light reflected from the moving beads. The sensitivity of the laser is checked by comparing the velocity of a shaker as measured by the laser with its acceleration as measured by a reference accelerometer.

Our surgical exposure of the stapes allowed nearly direct measurement of the piston-like component of stapes motion: the angle of the laser beam was about 30° relative to the piston direction. The volume velocity was estimated using the simplifying hypothesis of piston-like motion of the stapes (Figure 2.6). In this case, the volume velocity is simply the product of measured linear velocity and the average area of the chinchilla footplate (2 mm$^2$, Vrettakos *et al.*, 1988).

## 2.3 Compound Action Potentials

Hearing thresholds and cochlear health can be assessed, to some extent, by repeated measurements of Compound Action Potentials (CAP) along the experiment. The CAP is a sound-evoked potential due to the simultaneous firing of a large number of fibers of the auditory nerve. It is recorded by placing an electrode near the round window of the cochlea, measuring the potential difference with another electrode grounded in a neck muscle. CAP was measured in response to tone pips of increasing frequencies and increasing levels.

## 2.4 Animal Preparation

The main difficulty in the surgical approach is that the space near the vestibule is very small and difficult to access. Moreover, the middle ear ossicles are very small and fragile (for example, the area of the stapes footplate is about 2 mm$^2$), and any small alteration to these structures will result in a significant deficit in middle ear function, especially at high frequencies. Another potential problem is the proximity of the round window of the cochlea: touching it with a surgical tool could break the membrane and cause a leak in the inner ear fluid, resulting in flawed inner ear pressure measurements.

The surgical approach was determined based on the experience of the lab with chinchilla anatomy as well as preparatory work done on animal heads and skulls. In particular, we verified that a bony wall located dorso-medially with respect to the stapes footplate, bounded the vestibule. To verify this, we drilled a hole in this wall and pushed the stapes into the oval window; the footplate was then seen through the hole.

The animals were anesthetized with Nembutal and Ketamine. After a tracheotomy to facilitate respiration, an opening was made in the superior bulla. The tensor tympani muscle and the facial nerve that innervates the stapedius muscle were cut to prevent random contractions of these muscles during the experiment (Rosowski *et al.*, 2006). A second hole in the posterior bulla was made to view the stapes and round window. Part of the bony wall around the round window, in which the facial nerve passes, was removed in order to see the wall of the vestibule posterior to the stapes. In doing so, extreme care was taken to avoid pulling or damaging the stapedius tendon. A hole of approximate diameter 200 μm was made in the vestibule with a fine sharp pick for the fiber-optic pressure sensor (Figure 2.7).

The cartilaginous ear canal was cut and a brass tube was placed and glued in the bony ear canal to allow repeatable couplings of the earphone delivering the sound stimuli. The middle ear was open during the measurements.

## 2.5 Stimuli

A speaker is coupled to the brass tube in the ear canal. We use LabView software to construct stimuli and control the measurements of the voltage output of our different sensors. Both broadband chirps and stepped pure tones from 62.5 to 30 kHz are used.

## 2.6 Correction of Ear Canal Pressure Measurements

The middle ear pressure gain $G_{ME}$ is defined as the ratio between $P_V$ and $P_{TM}$, the pressure near the TM. A reference microphone built into the sound coupler provided measurements of ear-canal sound pressure ($P_{EC}$) at the entrance of the brass coupling tube, about 10 mm from the umbo (Figure 2.8). The sound pressure near the TM $P_{TM}$ is different from $P_{EC}$ at high frequencies. To account for these differences, we measured the transfer function $P_{TM}/P_{EC}$ in a dead ear, and multiplied our measured $P_{EC}$ with this

function. This correction affects our measurements of $G_{ME}$ and normalized stapes velocity ($U_S/P_{TM}$), but not $Z_C$, whose computation does not involve $P_{TM}$.

To measure this transfer function, we used the ear of a dead chinchilla, in which we performed the same surgical procedures as for a regular experiment (we opened the bulla, cut the tensor tympani and glued a brass tube coupler in the ear canal). We then drilled a 1 mm hole in the tympanic ring (bony structure supporting the TM), which we accessed from the posterior bulla hole. We inserted a ¼ inch probe tube microphone in the 1 mm hole and simultaneously measured sound pressure from the ¼ inch microphone near the TM, and from the ear-canal reference microphone 10 mm away. To avoid damaging the TM with the ¼ inch microphone, we inserted it in 0.5 mm steps, coming almost perpendicular to the longitudinal axis of the ear-canal. Measurements in response to pure tones, with the ¼ inch microphone placed from 0 to 2 mm away from the edge of the hole showed identical results on the entire range of measurement frequencies (62 Hz to 30 kHz). At 2.5 mm, both $P_{EC}$ and $P_{TM}$ increased in the low frequencies, consistent with a stiffening of the TM. We interpreted this change as the microphone touching the TM. When we backed up to 2 mm, the two pressures went back to the previous values. Visual confirmation of the location of the microphone showed that $P_{TM}$ measurements were done within 1 mm of the umbo. Moreover, in order to rule out the possibility that the recorded signal was coming from bone vibrations being transmitted to the ¼ inch microphone, which may have been in contact with the edges of the hole in which it was inserted, we sealed the probe tube of the microphone with a paper point, and repeated the measurements. The signal went down about 15 dB almost on the entire frequency range, which confirmed that we were measuring sound pressure in air and not bone vibrations.

The $P_{TM}/P_{EC}$ we measured is given in Figure 2.9. At frequencies below 3 kHz, the transfer function has a magnitude close to 0 dB and an angle close to 0 cycle: as expected, the two pressures are nearly identical at these low frequencies. At higher frequencies, the magnitude shows various peaks and notches. In particular, a large 11 dB notch can be seen at 12 kHz and a large 15 dB peak is present at 21 kHz. As for the angle, the overall trend is a decrease down to almost -1 cycle at 30 kHz, which is consistent with the propagation time of the sound wave between the locations of the two

microphones. In particular, the wavelength in air at 30 kHz is about 11 mm, which is close to the distance between the ear-canal microphone and the umbo (Figure 2.8).

## 2.7 Frequency Range

In earlier experiments, the earphone we used had a bad high-frequency response (roughly above 15 kHz). In that case, our high frequency measurements were not reliable. Therefore we restrict our results to the frequency range over which the measurements were above the noise floor, which we determined by testing the repeatability of both response magnitude and phase. In later experiments, we used another type of earphone with a good high-frequency response, and obtained good signal-to-noise ratios on the entire range of measurement frequencies, i.e. up to 30 kHz.

# 3. Results

13 animals were used in this study. Among these, 4 had their middle or inner ears damaged during surgery. In 2 other experiments the pressure sensor proved unstable. We therefore present $G_{ME}$ results in 7 animals. We simultaneously measured $V_S$ in 6 of these, so we present 6 sets of $Z_C$ measurements.

## 3.1 Middle Ear Pressure Gain $G_{ME}$

$G_{ME}$ was computed from simultaneous measurements of $P_V$ and $P_{EC}$, and corrected for each animal to account for the differences between $P_{TM}$ and $P_{EC}$, as explained in the Methods.

$P_V /P_{EC}$ is plotted in Figure 3.1. Both magnitude and angle were similar among the 7 ears. The standard deviation was between 4 and 10 dB for the magnitude over almost the entire frequency range of measurement, and less than 0.1 cycle for the angle below 8 kHz. The average $|P_V /P_{EC}|$ across these 7 ears was between 20 and 40 dB between 100 Hz and 10 kHz. It increased from 17 dB to 34 dB with frequency between 62-400 Hz, slowly decreased to 25 dB with frequency between 400-2500 Hz, increased sharply to reach a 35 dB maximum at 6 kHz, decreased sharply to reach a 7 dB minimum at 17 kHz, and slightly increased to 10-12 dB at 30 kHz. The average angle decreased from 0.4 to 0 cycles with frequency 62-300 Hz, was near 0 between 0.3 and 3 kHz, and accumulated with frequency above that, reaching -0.8 cycles by 10 kHz and -1.4 cycle by 30 kHz.

The corrected middle ear gain $G_{ME} =P_V /P_{TM}$ is very similar to $P_V /P_{EC}$ below 3 kHz (Figure 3.2). Both magnitude and angle show larger differences at high frequencies, as expected given the correction function $P_{TM} /P_{EC}$ (see Figure 2.9). $|G_{ME}|$ has a larger maximum than $|P_V /P_{EC}|$ (40 dB instead of 35 dB) at a slightly lower frequency (5 kHz instead of 6 kHz). The sharp decrease between 6 kHz and 17 kHz is similar in both cases. Instead of a notch at 17 kHz, $|G_{ME}|$ reaches its minimum at a higher frequency (20 kHz) with a lower value (-4 dB). The angle of $G_{ME}$ is close to 0 on a wider range of frequency (up to about 4 kHz), before accumulating with the same rate as $P_V /P_{EC,}$ reaching -0.9 cycles at 13 kHz. Between 13 and 30 kHz, the two angles are significantly different: $G_{ME}$'s angle has a complicated shape but roughly increases to a value of -0.4 cycles.

## 3.2  Stapes Volume Velocity $U_S$

$U_S$ (Figure 2) was computed from the stapes velocity $V_S$ and a mean stapes footplate area as described in the methods, and normalized by $P_{EC}$. $V_S$ was measured before and after the vestibular hole was made and the pressure sensor inserted in the vestibule. In both conditions, the $U_S/P_{EC}$ ratio was corrected by the $P_{TM}/P_{EC}$ transfer function.

### 3.2.1  Intact vestibule

$U_S/P_{EC}$ (Figure 3.3) was similar among 6 ears. The standard deviation was less than $10^{-10}$ $m^3$/(s-Pa) for the magnitude, and less than 0.1 cycle for the angle, on most of the frequency range of measurement. $|U_S/P_{EC}|$ increased with frequency 60–300 Hz and the angle was near +0.25 cycles, consistent with a compliance. $|U_S/P_{EC}|$ decreased slightly with frequency 0.3–2 kHz and the angle was between 0 and -0.25 cycles, consistent with a mass-resistance combination. $|U_S/P_{EC}|$ increased slightly with frequency 3–7 kHz, decreased with frequency 7-12 kHz, and the angle decreased toward -1.2 cycles. Between 12 and 30 kHz, $|U_S/P_{EC}|$ is characterized by a notch centered at 17 kHz; the angle further decreased, reaching -1.8 cycles by 30 kHz.

The corrected normalized volume velocity $U_S/P_{TM}$ is very similar to $U_S/P_{EC}$ below 3 kHz (Figure 3.4).The differences observed at higher frequencies are similar to the differences between $G_{ME} = P_V/P_{TM}$ and $P_V/P_{EC}$ described above. In particular, $|U_S/P_{TM}|$ reaches a larger maximum at 5 kHz, and a lower minimum at 20 kHz. The angle is also larger overall, with a maximum difference at 30 kHz with a value of -1.2 instead of -1.8 cycles.

### 3.2.2  With vestibular hole and microphone in place

$U_S/P_{EC}$ (Figure 3.5) and $U_S/P_{TM}$ (Figure 3.6) are very similar to the intact vestibule condition. The standard deviation of the magnitude is smaller for the condition with an intact vestibule. The effect of the hole will be discussed more in the Discussion section.

## 3.3  Cochlear Input Impedance $Z_C$

### 3.3.1  Fixed level

$Z_C$ (Figure 3.7) was computed from simultaneous measurements of $P_V$ and $U_S$. The computation of $Z_C$ does not use $P_{TM}$, therefore our results are not affected by the correction employed to convert $P_{EC}$ to $P_{TM}$. $Z_C$ was similar among 6 ears, besides a low outlier for $|Z_C|$ in one ear at low frequencies and a low outlier in a different ear at high frequencies.

The average $|Z_C|$ was about $10^{11}$ acoustic ohms, roughly constant with frequency up to 10 kHz, increased sharply from 10–20 kHz and fell sharply from 20–30 kHz. The angle was near zero below 10 kHz, which corresponds to the frequency range where $|Z_C|$ was nearly flat. This is consistent with a resistance.

The angle had values between –0.25 and +0.25 cycles at all frequencies measured except where it was contaminated by noise. This is consistent with the input impedance of a passive system

### 3.3.2  Linearity with level

In 2 experiments, we repeated the $Z_C$ measurements with different sound pressure levels, in order to explore the linearity of $Z_C$ with level. We observed small changes at very low and very high frequency, but these changes were due to measurement noise: The noise floor for the Laser Doppler measurement system has a "V" shape as a function of frequency, and decreasing the sound level had the effect to lower the laser response, which reached the noise floor at low and high frequencies. There was no change at frequencies over which the signal-to-noise ratio was good at every level.

# 4. Discussion

## 4.1 High Frequency Responses

The high frequency responses we obtained for $G_{ME}$ and normalized $U_S$ are characterized by an increased variance in magnitude and/or angle relative to lower frequencies. For $G_{ME}$, the standard deviation was about 15 dB above 20 kHz for the magnitude, and as large as 0.5 cycles between 25 and 30 kHz for the angle (Figure 3.2). For normalized $U_S$, the variance of the magnitude above 20 kHz is similar to lower frequencies, but the standard deviation of the angle grows to 1.5 cycles (Figures 3.4 and 3.6).

These increased variances are not due to measurement noise, because only responses with good signal-to-noise ratios were kept. They can be explained by at least two factors:

- In earlier experiments, the earphone we were using did not provide a good signal-to-noise ratio at high frequency, so there are only 3 ears with good signal-to-noise ratio above 16 kHz. We need to repeat the measurements in more individuals to have better estimates of the mean response at high frequencies.

- For $U_S$, we are assuming piston-like motion of the stapes, and measuring velocity in only one direction. For piston-like motion, the responses are not very sensitive to the laser beam angle, at least for angles below 45°. For example, measuring with a 30° angle relative to the piston axis introduces an error corresponding to a factor of $\cos(30°) = \dfrac{\sqrt{3}}{2} \approx 0.87$ or -1.2 dB in measuring the piston component, whereas a 45° angle will produce a -3 dB error and a 20° angle will result in a -0.5 dB error. During an experiment, the laser angle was set so as to have a clear view of reflectors on the stapes footplate or posterior crus. The actual measurement angle was therefore highly dependent upon the animal's specific anatomy and position of the reflectors, usually between 20° and 45°. If stapes motion was truly piston-like, the uncertainty on the measurement angle would only result in less than a 3 dB error for these angle values. However, it is unlikely that the assumption of piston-like motion is valid at high frequencies, and other motion modes may be emphasized by our measurement angles. The existence of such

24

multiple modes of motion at high frequency could explain the larger variance for $U_S$ and consequently for $Z_C$ in that frequency range.

The notch we found in normalized $U_S$ between 12 and 30 kHz, as well as the sharp peak in $|Z_C|$ at these frequencies (Figures 3.4, 3.6 and 3.7), can also be explained by complex motion of the stapes at high frequency. A hypothesis is that the rocking component of stapes motion around 20 kHz is very important, which would result in a measured linear motion of significantly lesser amplitude considering the angle of the laser beam with the footplate. This hypothesis is credible in light of a study by Heiland *et al.* (1999), who measured the 3D motion of the stapes footplate in human temporal bones, and found that piston-like motion was predominant at low frequencies (below 4 kHz), but that rocking and piston-like motions were comparable at 4 kHz. The Heiland study cannot describe the frequencies over which rocking motion occurs in chinchillas, because the motion of the stapes certainly is species-specific.

Finally, another possible source of imprecision at high frequency is the transfer function we used to correct for differences between $P_{TM}$ and $P_{EC}$. The peaks and valleys observed, in particular above 10 kHz, are dependent upon the anatomy of the ear-canal, which varies among individuals. Consequently, we can expect the correction to be imperfect.

## 4.2 Influence of the Vestibular Hole

### 4.2.1 Experimental changes in normalized $U_S$ and $G_{ME}$

It was necessary to make a hole in the vestibule to introduce the pressure sensor and measure $P_V$. To assess the influence of the hole on $U_S/P_{TM}$, we compared measurements of $U_S/P_{TM}$ before the hole was made and afterward with the pressure sensor in place. We found a small (< 7 dB) increase in $|U_S/P_{TM}|$ in the condition with the vestibular hole (Figure 4.1), which is consistent with the hole decreasing cochlear input impedance and facilitating stapes motion. A Student's t-test performed at each frequency showed that the changes were significant (p<0.01) only in a small region around 8 kHz.

To determine the influence of the hole around the inserted pressure sensor on $G_{ME}$, we tried to seal the pressure sensor in place with dental impression material (Jeltrate), dental cement, or a sodium hyaluronate viscoelastic gel of high molecular weight (Healon GV

14 mg/mL). In most preparations, it was not possible to seal around the sensor effectively because of the limited space available and because the outward flow of perilymph pushed the sealant material away. In one case shown in Figure 4.2, the Healon GV gel appeared to cover most of the hole, resulting in an increase in $P_V$, and therefore in $G_{ME}$, especially at frequencies below 1 kHz (by as much as 15 dB at 150 Hz). After removing the gel, $P_V$ went back to the lower level. Several other attempts at sealing the hole produced smaller changes.

Overall, the effects of the vestibular hole on $G_{ME}$ and $U_S/P_{TM}$ were small and limited in frequency. The changes we observed for $U_S/P_{TM}$ were consistent with a study by Songer and Rosowski (2006). In this study, they looked at the effect of semi-circular canal dehiscence on $U_S/P_{TM}$, in chinchillas. They found that the change in $U_S/P_{TM}$ was maximal at frequencies 150-500 Hz (5-10 dB), decreased with frequency 500-1000 Hz to a value of roughly 2 dB, and stayed at this lower value from 1-7 kHz. Measurements were noisy above 7 kHz. In our study, the change in $U_S/P_{TM}$ had a similar shape below 1 kHz, but had a lower value (the maximum of the mean was about 5 dB at these frequencies) and was not statistically significant. The significant changes we observed around 8 kHz are not visible in Songer and Rosowski's study, but this could be because of their noise issue at these high frequencies, or simply because of differences in the experimental setup: We introduced a small (200-250 μm diameter) partially plugged (by a 170 μm diameter pressure sensor) hole in the vestibule, whereas they introduced a larger (500 μm diameter) open hole in the superior semi-circular canal. Nonetheless, the smaller change we observed at low frequencies (5 dB on average in our case, ~10 dB in their study) is consistent with the smaller hole we introduced.

It was not possible to determine whether part of the changes we measured in $G_{ME}$ and $U_S/P_{TM}$ were due to changes in $P_{TM}$: Comparison of the measured $P_{TM}$ before the hole is made and afterward is not valid because we had to move the animal head to make the hole, resulting in a slightly different seal of the ear-phone in the brass-tube coupler, which affects $P_{TM}$.

### 4.2.2 Predictions by an acoustic model

As plugging the hole around the pressure sensor was difficult, and as we only have data for changes in $G_{ME}$ in one animal, we used a lumped-element acoustic model to provide further insight on the influence of the hole.

#### 4.2.2.1 Acoustic model

The model we used to investigate the effect of the open hole around our $P_V$ sensor (Figure 4.3) represents the middle ear as a Norton equivalent circuit, providing volume velocity $U_S$ to the parallel combination of the inner ear load ($Z_C$) and the impedance of the hole ($Z_{HOLE}$). The Norton equivalent is composed of an ideal volume velocity source and the output impedance of the middle ear ($Z_{OUT}$). The pressure across each of the parallel branches of the circuit is $P_V$.

The changes in $P_V$ and $U_S$ introduced by opening the hole can be inferred from this circuit by the simple linear equations of current dividers. We obtained:

$$\frac{P_{V\_hole}}{P_{V\_normal}} = 1 - \frac{Z_C Z_{OUT}}{Z_C Z_{OUT} + Z_C Z_{HOLE} + Z_{HOLE} Z_{OUT}}$$

$$\frac{U_{S\_hole}}{U_{S\_normal}} = 1 + \frac{Z_C^{\ 2}}{Z_C Z_{OUT} + Z_C Z_{HOLE} + Z_{HOLE} Z_{OUT}}$$

If we further assume that $P_{TM}$ does not depend on the presence of the hole, these ratios also represent the change in $G_{ME}$ and $U_S/P_{TM}$. We were not able to determine whether this assumption is valid for the small dimension holes we introduced, as explained in 4.2.1.

#### 4.2.2.2 Estimates of the model elements

These ratios depend on three unknown impedances: $Z_C$, $Z_{OUT}$ and $Z_{HOLE}$. We used estimates of $Z_C$ and $Z_{OUT}$ by Songer and Rosowski (2007a), which they computed based on a transmission matrix model of the middle ear, fed by measurements of ear-canal pressure and tympanic membrane velocity in chinchillas below 8 kHz. To compute $Z_{HOLE}$, we modeled the hole by a lossy transmission line. This model was originally

developed by Egolf (1977), and used to model fluid-filled tube segments by Songer and Rosowski (2007b). In our case, $Z_{HOLE}$ is computed as follows:

$$Z_{HOLE} = \frac{Az_0 + B}{Cz_0 + D}$$

with $z_0$ the termination impedance of the hole, and A, B, C, D parameters depending on various thermodynamic parameters of the medium, frequency, and the dimensions of the hole. A detailed description of these parameters can be found in Songer and Rosowski (2007b).

The original model is for a tube of radius $a$ and length $l$. For our purpose, this description is not entirely satisfying because the hole is partially obstructed by the pressure sensor. In order to apply the model, we computed an "equivalent radius" corresponding to the radius of a hole of cross-section area equal to the area of the annulus delimited by the pressure sensor and the circular edge of the hole. Specifically:

$$a_{equivalent} = \sqrt{a^2 - a_{sensor}^2}$$

with $a_{sensor} = \dfrac{170}{2} = 85\,\mu m$ the radius of the pressure sensor.

During the experiments, making the hole usually resulted in perilymph leaking out from the cochlea at a slow rate. Therefore, the termination impedance $z_0$ that we used was the mass of the fluid terminating the tube.

### 4.2.2.3  Comparison of the predicted results with the experimental data

The results obtained with this model share similarities with the experimental data. Introducing a 200 μm diameter hole reduced $|P_V|$ near 150 Hz by about 10-12 dB, which is consistent with the 10-15 dB increase in the experimental data upon introduction of the gel to seal the hole (See Figure 4.2). The effect of the hole was smaller as frequency increased, with less than a 3 dB difference by 1 kHz in both the experimental and predicted data. Nonetheless, the detailed shape of the predicted change in $|P_V|$ is different from the measured change, as expected given the simplicity of the model. As for the angle, the ~0.15 cycle increase predicted by the model at 150 Hz is consistent with the experimental data around this frequency, but the measured and predicted changes differ slightly at other frequencies.

The predicted changes in $U_S$ are very small: the change in angle was close to 0 over the entire frequency range of the data (except the first data point at 62 Hz), and the change in magnitude was less than 1 dB below 1.5 kHz, and between 1 and 2 dB at frequencies 1.5-8 kHz (except for a small notch at -1 dB at 2.5 kHz). This is consistent with the experimental data over a wide range of frequencies (see Figure 4.1): The average change in 6 animals was about 5 dB in magnitude below 6 kHz, but not statistically significant at these frequencies, and the angle was close to 0. Nonetheless, the slightly larger and significant experimental changes obtained between 6 and 8 kHz were not seen in the predicted data. The experimental changes observed between 8 and 10 kHz could not be compared with the model, because the measurements used to constrain the model's cochlear input impedance had an upper range limit of 8 kHz.

To conclude: The predictions of this simple model were at least qualitatively similar to the experimental data: $P_V$ changes were maximal in the low frequencies, and $U_S$ did not change much over most of the frequency range. This is consistent with the error introduced by the hole being small, except maybe for frequencies around 150 Hz in the case of the $P_V$ measurements.

## 4.3 Comparison with other Studies

### 4.3.1 In the chinchilla

We talked in the Background section about a simple ideal transformer model of the middle ear. A theoretical anatomical "transformer ratio" can be computed as the product of the "area ratio" (the area of the TM divided by the area of the stapes footplate) and the "lever ratio" (malleus length divided by incus length). Anatomical values in the chinchilla from Fleischer (1973) and Vrettakos *et al.* (1988) lead to an "area ratio" of 29 dB and a "lever ratio" of 6 dB. The total "transformer ratio" is therefore 35 dB. It is interesting to note that $|G_{ME}|$ was comparable to this "transformer ratio" of 35 dB (see Figure 3.2) over a wide frequency range (roughly 300 Hz to 4 kHz). Moreover, the angle was close to 0 in the same frequency range, which is also consistent with the ideal transformer model.

Our $G_{ME}$ results are very similar to a previous study by Décory (1989) in chinchilla between 500 Hz and 3 kHz, for both the magnitude and the angle (Figure 4.5). Moreover,

the slightly negative slope of $|G_{ME}|$ at these frequencies was similar in both cases. In the same frequency range, the angle we measured was closer to 0 than Décory's, but the two did not differ by more than 0.1 cycle. Below 500 Hz, and between 3 kHz and 10 kHz, we found a larger $|G_{ME}|$. The fall in $|G_{ME}|$ we found between 12 and 20 kHz resembles the roll off in Décory's data at about the same frequencies. The notch in the angle that we found at 13 kHz did not appear in Décory's data, but the two rejoined at 20 kHz.

Our measurements of normalized $U_S$ compare very well with a study by Songer and Rosowski (2007a) in magnitude as well as angle (Figure 4.6). Our results are also very similar to those of Ruggero *et al.* (1990) at frequencies below 12 kHz. The small differences in magnitude between ours and the Ruggero study may be due to the correction they applied to take into account that the tensor tympani muscle was cut. Differences in the experimental setup may also explain some variations. The large notch we found between 12 and 30 kHz is in contradiction with another study by Ruggero *et al.* (2007), in which they measured ossicular vibrations in chinchillas up to 40 kHz and obtained a roughly flat magnitude for the normalized $U_S$ at least up to 25 kHz. As we discussed earlier, our high frequency results are not as reliable as the lower frequency range of our data, which could explain the difference. Another potential reason for these differences at high frequency is that they measured velocity of the lenticular process, and added gains measured across the incudo-stapedial joint, whereas we measured velocity from locations on the footplate and parts of the crua close to the footplate.

We compared our $Z_C$ measurements with a model by Songer and Rosowski (2007a), as well as computations by Ruggero *et al.* (1990), who used their own $U_S$ measurements and Décory's $P_V$ measurements in other animals (see Figure 4.5). The 3 data sets share many similarities (Figure 4.7): In particular, the impedances are mostly resistive with an order of magnitude of about $10^{11}$ acoustic ohms. The differences in magnitude between our data and Ruggero *et al.*'s below 500 Hz and between 3 and 10 kHz are consistent with the larger $G_{ME}$ we measured at these frequencies.

### 4.3.2   In other species

$G_{ME}$ is shown for chinchilla (our data) along with cat, guinea pig (from Décory, 1989), gerbil (from Olson, 1998) and human temporal bone (from Puria *et al.*, 1997) in Figure

30

4.8. $|G_{ME}|$ is largest for the chinchilla, especially at low frequencies, but the magnitudes of all these species are similar (within 10 dB) for frequencies between 500 Hz and 3 kHz.

Except for human temporal bone, the overall shape of $|G_{ME}|$ can be consistently described in these species by two more or less broad lobes followed by a sharp roll-off. For chinchilla, the first lobe is wide (from 62 to 2 kHz) and the second one (2 kHz to 13 kHz) peaks at a larger value (about 40 dB). For cat and guinea pig, the first lobe has a larger maximum than the second one (about 32 dB for cat and 31 dB for guinea pig). The separation between the two lobes is more prominent in the cat data (large notch centered at 3 kHz). The high-frequency roll-off for the guinea pig is similar to the chinchilla. For the cat, the roll-off occurs at slightly lower frequencies (0 dB is reached by 15 kHz). For the gerbil data, the separation between the two lobes is at about 7 kHz), but the second lobe extends to at least 46 kHz (data not shown in Figure 4.8) and there is no evidence of a roll-off at these frequencies.

The angles of $G_{ME}$ in these species have similarities in shape, but the decrease with frequency varies across species (fastest for the cat, slowest for the gerbil).In our data in chinchilla as well as for cat and guinea pig, the angle increases slightly at high frequency after reaching a minimum. It is difficult to tell whether this increase is real or if the phase should be unwrapped differently, for example by adding an extra cycle at high frequencies. This could be determined by remeasuring with a higher high frequency resolution.

As for $Z_C$ (Figure 4.9), we compared our measurements with data in cat (from Lynch *et al.*, 1994), guinea pig (from Dancer and Franke, 1980), gerbil (from de la Rochefoucauld *et al*., 2008) and human temporal bone (from Aibara *et al*., 2001). Chinchilla and cat are very similar up to 8 kHz for both magnitude and angle. For all these species, the magnitudes are approximately flat and the angles close to 0.

## 4.4 Can the Audiogram be Explained by the Acoustic Power Delivered to the Cochlea?

We wanted to test the hypothesis that the auditory thresholds are primarily determined by the average acoustic power delivered to the cochlea $W_C$. This quantity can be related to the cochlear input impedance $Z_C$ as follows:

$$W_C = \frac{1}{2}\Re\{P_V U_S^*\} = \frac{1}{2}|P_V|^2 \Re\left\{\frac{1}{Z_C}\right\}$$

Therefore, for a particular pressure at the TM $P_{TM}$, we can compute the average power $W_C$ thanks to our measurements of $P_V$ and $U_S$. An auditory threshold is defined as the minimum pressure needed to elicit a sensation. Therefore we computed the pressure $P_{TM}$ per unit power at the entrance to the cochlea in order to compare this quantity to the auditory thresholds. Originally, we wanted to determine the auditory thresholds based on CAP in each animal and make the comparison for each individual. This did not prove possible, because the CAP thresholds we obtained were very high, especially at high frequency, in contradiction with the auditory thresholds found in the literature. An explanation for this hearing loss is that the base of the cochlea was exposed at room temperature, which is known to inhibit cochlear activity.

Instead of an individual comparison, we compared the average pressure per unit power at the entrance to the cochlea to an average audiogram from the literature (from Miller, 1970). A complication was that Miller's audiogram was measured in free field, whereas our experiments were done with the sound stimuli delivered directly in the ear-canal. To account for the differences between free field pressure $P_{FF}$ and ear-canal pressure near the TM $P_{TM}$, we used an average Head Related Transfer Function (HRTF) measured in the chinchilla by von Bismark and Pfeiffer (1967). This HRTF quantifies in particular the filtering effect of the head and pinnae on the incoming sound.

Figure 4.10 shows Miller's audiogram, the pressure at the TM per acoustic power in the vestibule $|P_{TM}|/W_C$, and the same quantity in free field after correction by the chinchilla HRTF, $|P_{FF}|/W_C$. The HRTF was available between 250 Hz and 8 kHz, which limited the range of $|P_{FF}|/W_C$, Nonetheless, given the wavelength of sound at low frequencies in comparison to the size of the head and pinnae, we can assume that the HRTF has a 0 dB gain below 250 Hz, and therefore the $|P_{TM}|/W_C$ approximates well $|P_{FF}|/W_C$ below 250 Hz. The comparison between $|P_{FF}|/W_C$ (or $|P_{TM}|/W_C$ in the low frequencies) with the audiogram is excellent at frequencies below 250 Hz, and less than 5 dB up to about 1 kHz. Between 1 and 8 kHz, there are more significant differences: the audiogram is almost flat with thresholds between 0 and 5 dB SPL, whereas $|P_{FF}|/W_C$ increases to a maximum around 2 kHz and decreases to a minimum around 5 kHz, with

differences of about 5 to 15 dB from the audiogram. Above 8 kHz, the free field correction was not available, but $|P_{TM}|/W_C$ increased significantly sharper than the audiogram.

Consequently, the power delivered to the cochlea was very well correlated to the audiogram in the low frequencies (below 1 kHz), but not at higher frequencies. Nonetheless, we can notice that $|P_{FF}|/W_C$ was in the same range as the audiogram between 1 and 7 kHz.

# 5. Conclusions

In this project, we built stable fiber-optic pressure sensors, calibrated them, and showed that it was possible to measure sound pressure in the vestibule of chinchillas while limiting the errors due to our experimental setup. In particular, the introduction of a hole in the vestibule, necessary to insert the sensors, had only little influence on the middle ear pressure gain and the normalized stapes velocity. This was shown based on comparisons between measurements with an intact vestibule (or with the hole plugged with a viscous gel) and measurements with the hole open and the pressure sensor in place. A lumped-element model using a volume velocity source loaded by the output impedance of the middle ear, the input impedance of the cochlea, and the impedance of the hole, provided qualitatively similar results.

Other potential sources of error at high frequencies were identified. First of all, the ear-canal reference pressure $P_{EC}$ was measured too far away from the tympanic membrane; we accounted for the differences with $P_{TM}$ by correcting our results with the appropriate transfer function. Another source of error came from our assumption of piston-like motion of the stapes and the angle with which we measured stapes velocity.

Our measurements of middle ear pressure gain were similar to published data in the chinchilla at stimulus frequencies of 500 Hz to 3 kHz, but we obtained larger gains at low frequencies and between 3 and 10 kHz. Our average pressure gain was similar to the gain predicted by the ideal transformer model of the middle ear on a broad range of frequencies, with a magnitude of the order of 35 dB and an angle near 0. Our measurements of cochlear input impedance differed somewhat from previous estimates in the chinchilla and showed a resistive input impedance up to at least 10 kHz, and a magnitude of the order of $10^{11}$ acoustic ohms. To our knowledge, these are the first direct measurements of this impedance in the chinchilla.

The acoustic power entering the cochlea was computed based on our measurements of input impedance. This quantity was a good predictor for the audiogram at frequencies below 1 kHz.

# References

Aibara R., Welsh J.T., Puria S. and Goode R.L. (2001): *Human middle ear sound transfer function and cochlear input impedance*, Hear. Res. 152(1-2):100-109

Beranek L.L. (1996): *Acoustics*, pubished by the Acoustical Society of America.

von Bismark G. and Pfeiffer R.R. (1967): *On the sound pressure transformation from free field to eardrum of chinchilla*, J. Acoust. Soc. Am. Suppl. 1, 42, S156.

Borg E. and Zakrisson J. E. (1973): *Stapedius reflex and speech features*, J. Acoust. Soc. Am. 54:525–527.

Cook R.O. and Hamm C.W. (1979): *Fiber optic lever displacement transducer*, Applied Optics 18(19):3230-3241.

Dancer A. and Franke R. (1980): *Intracochlear sound pressure measurements in guinea pigs*, Hear. Res. 2(3-4):191-205.

Décory L. (1989): *Origine des différences interspécifiques de susceptibilités au bruit*, Thèse de Doctorat de l'Université de Bordeaux, France.

Egolf D.P. (1977): *Mathematical modeling of a probe-tube microphone*, J. Acoust. Soc. Am. 61(1):200-205.

Fleischer G. (1973): *Studien am Skelett des Gehörorgans der Säugetiere, einschliesslich des Menschen, Säugetierkundl*, Mitteilungen (München) 21:131-239

Heiland K.E., Goode R.L., Asai M. and Huber A.M. (1999): *A human temporal bone study of stapes footplate movement*, Am. J. Otol. 20(1):81-6.

von Helmholtz H.L. (1877): *The sensation of tones*, New York: Dover.

Lynch T.J. 3rd, Peake W.T. and Rosowski J.J. (1994): *Measurements of the acoustic input impedance of cat ears: 10 Hz to 20 kHz,* J. Acoust. Soc. Am. 96(4):2184-2209

Miller J.D. (1970): *Audibility curve of the chinchilla*, J. Acoust. Soc. Am. 48:513- 523.

Nedzelnitsky V. (1980): *Sound pressures in the basal turn of the cat cochlea*, J. Acoust. Soc. Am. 68:1676-1689.

Olson E.S. (1998): *Observing middle and inner ear mechanics with novel intracochlear pressure sensors*, J. Acoust. Soc. Am. 103(6):3445-3463.

Puria S., Peake W.T. and Rosowski J.J. (1997): *Sound-pressure measurements in the cochlear vestibule of human-cadaver ears*, J. Acoust. Soc. Am. 101(5 Pt 1):2754-2770

de la Rochefoucauld O., Decraemer W.F., Khanna S.M. and Olson, E.S. (2008): *Simultaneous measurements of stapes motion and intracochlear pressure in gerbil from 0.5–50 kHz*, J. Assoc. Res. Otolaryngol., in press.

Rosowski J.J. (1991): *The effects of external and middle ear filtering on auditory threshold and noise-induced hearing loss,* J. Acoust. Soc. Am. 90:124-135.

Rosowski J.J. (1994): *Outer and Middle Ears*, in Fay R.R. and Popper A.N. (Eds.), *Comparative Hearing: Mammals*, pp. 172-247, Springer-Verlag, New York.

Rosowski J.J. (1996): *Models of External and Middle Ear Function*, in Hawkins H.L., McMullen T.A., Popper A.N. and Fay R.R.(Eds.), *Auditory Computation*, pp. 15-61, Springer, New York.

Rosowski J.J., Ravicz M.E. and Songer J.E. (2006): *Structures that contribute to middle-ear admittance in chinchilla,* J. Comp. Physiol. A. 192:1287-1311.

Ruggero M.A., Rich N.C., Robles L. and Shivapuja B.G. (1990): *Middle ear response in the chinchilla and its relationship to mechanics at the base of the cochlea*, J. Acoust. Soc. Am. 87(4):1612-1629.

Ruggero M.A., Temchin A.N., Fan Y.-H. and Cai H. (2007): *Boost of transmission at the pedicle of the incus in the chinchilla middle ear*, Middle Ear Mechanics in Research and Otology, Proceedings of the 4th International Symposium, pp. 154-157, World Scientific

Songer J.E. and Rosowski J.J. (2006): *The effect of superior-canal opening on middle ear input admittance and air-conducted stapes velocity in chinchilla,* J. Acoust. Soc. Am. 120(1):258-269.

Songer J.E. and Rosowski J.J. (2007a): *Transmission matrix analysis of the chinchilla middle ear,* J. Acoust. Soc. Am. 122(2):932-942.

Songer J.E. and Rosowski J.J. (2007b): *A mechano-acoustic model of the effect of superior canal dehiscence on hearing in chinchilla,* J. Acoust. Soc. Am. 122(2):943-951.

Puria S. and Allen J.B. (1998): *Measurements and model of the cat middle ear: Evidence of tympanic membrane acoustic delay,* J. Acoust. Soc. Am. 104:3463-3481.

Schloss F. and Strasberg M. (1962): *Hydrophone Calibration in a Vibrating Column of Liquid*, J. Acoust. Soc. Am. 34(7):958-960.

Vrettakos P.A., Dear S.P. and Saunders J.C. (1988): *Middle ear structure in the chinchilla: A quantitative study*, Am. J. Otolaryngol. 9:58-67.

# Figures



© Northwestern University

External auditory canal

Inner Ear

Outer Ear

Middle Ear

| | | |
|---|---|---|
| 1. Eardrum | 5. Semicircular canals | 8. Vestibular nerve |
| 2. Malleus | 6. Auditory nerve | 9. Cochlea |
| 3. Incus | 7. Facial Nerve | 10. Eustachian tube |
| 4. Stapes | | |
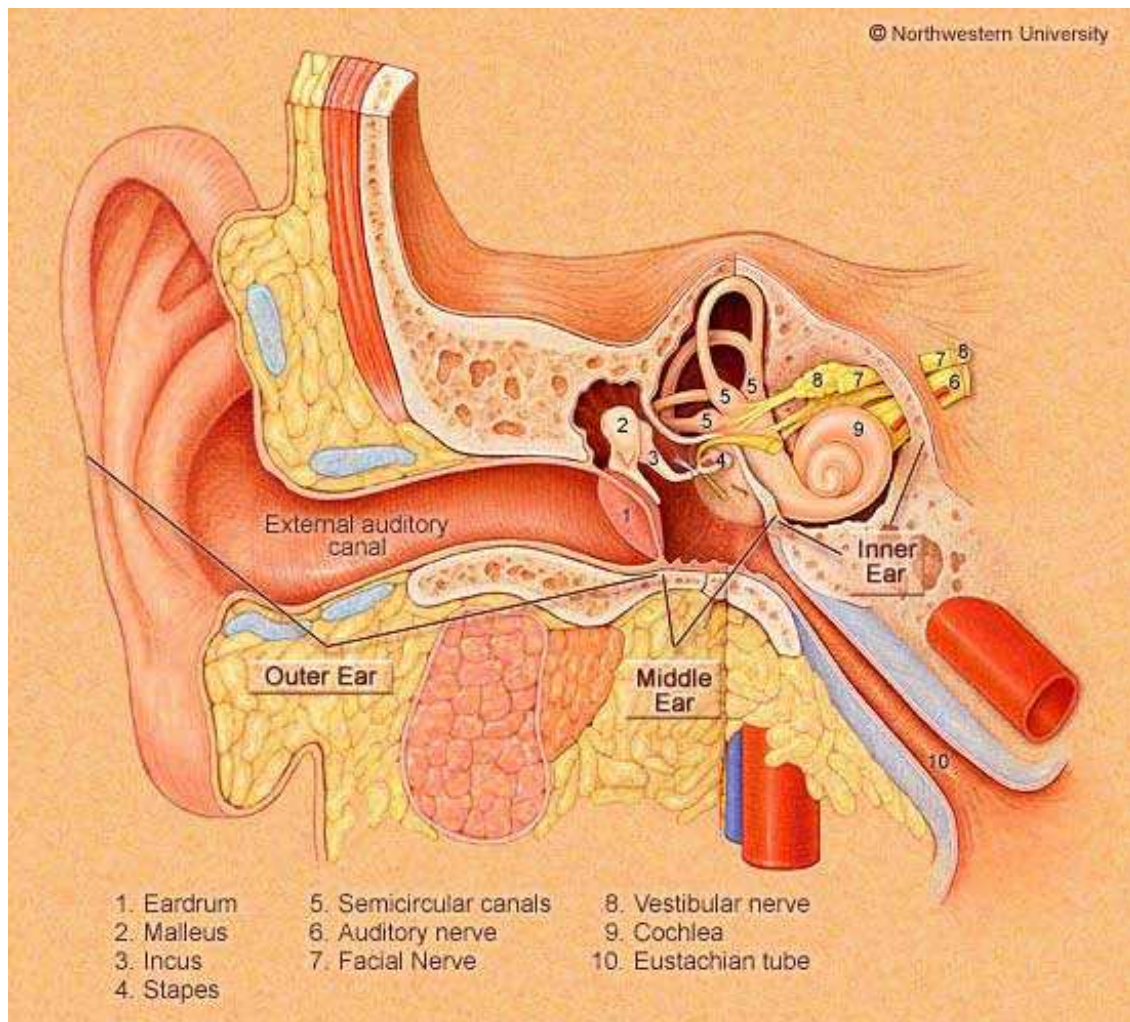
**Figure 1.1:** The subdivisions of the peripheral auditory system into outer, middle and inner ears in human (from Northwestern University).
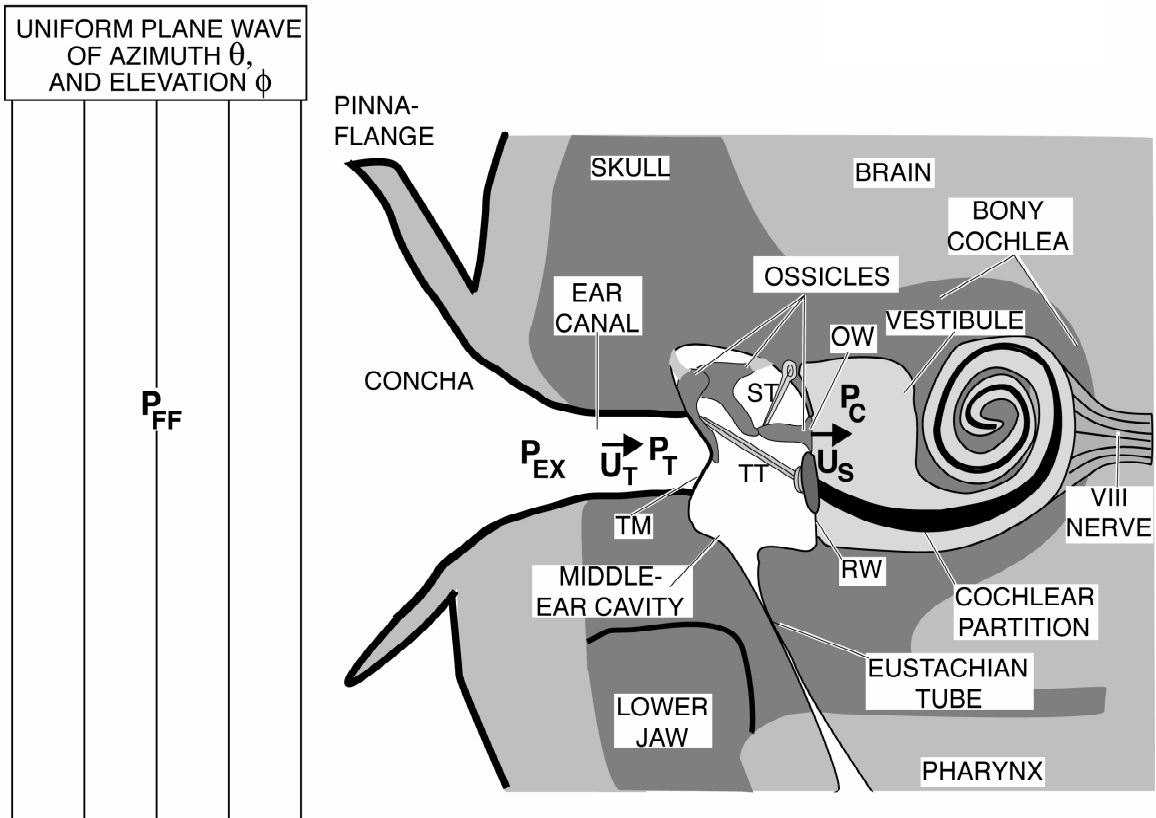
**Figure 1.2:** Schematic representation of the auditory periphery of a terrestrial mammal and variables of interest (from Rosowski, 1991).
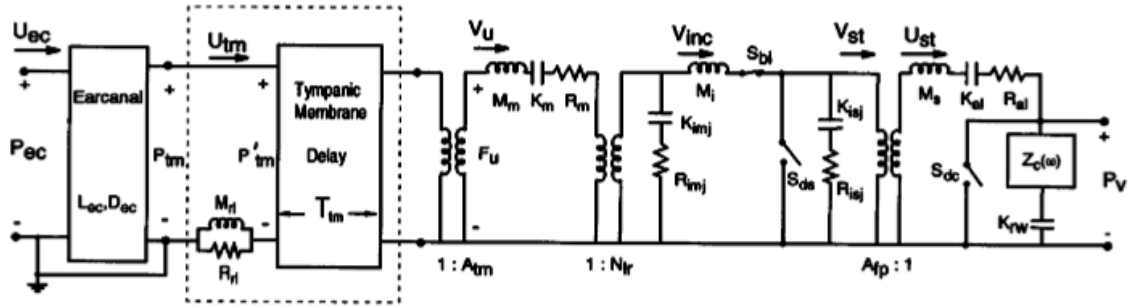
**Figure 1.3:** Lumped-element model of the cat middle ear (from Puria and Allen, 1998).
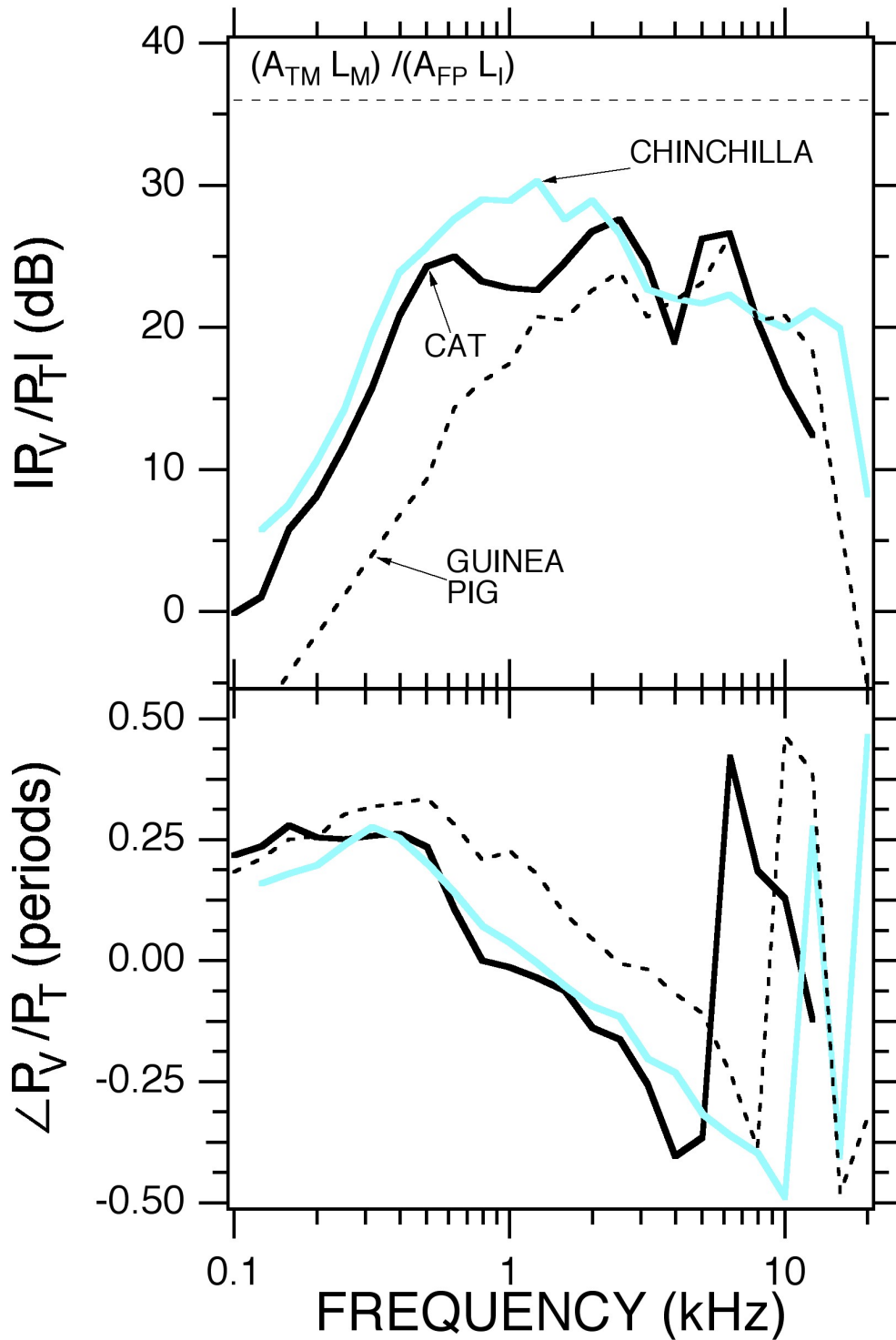
**Figure 1.4:** Middle Ear Gain in chinchilla (from Décory 1989), cat (from Nedzelnitsky 1980), guinea pig (from Dancer and Franke, 1980), and ideal transformer model for the chinchilla (after Rosowski, 1994).
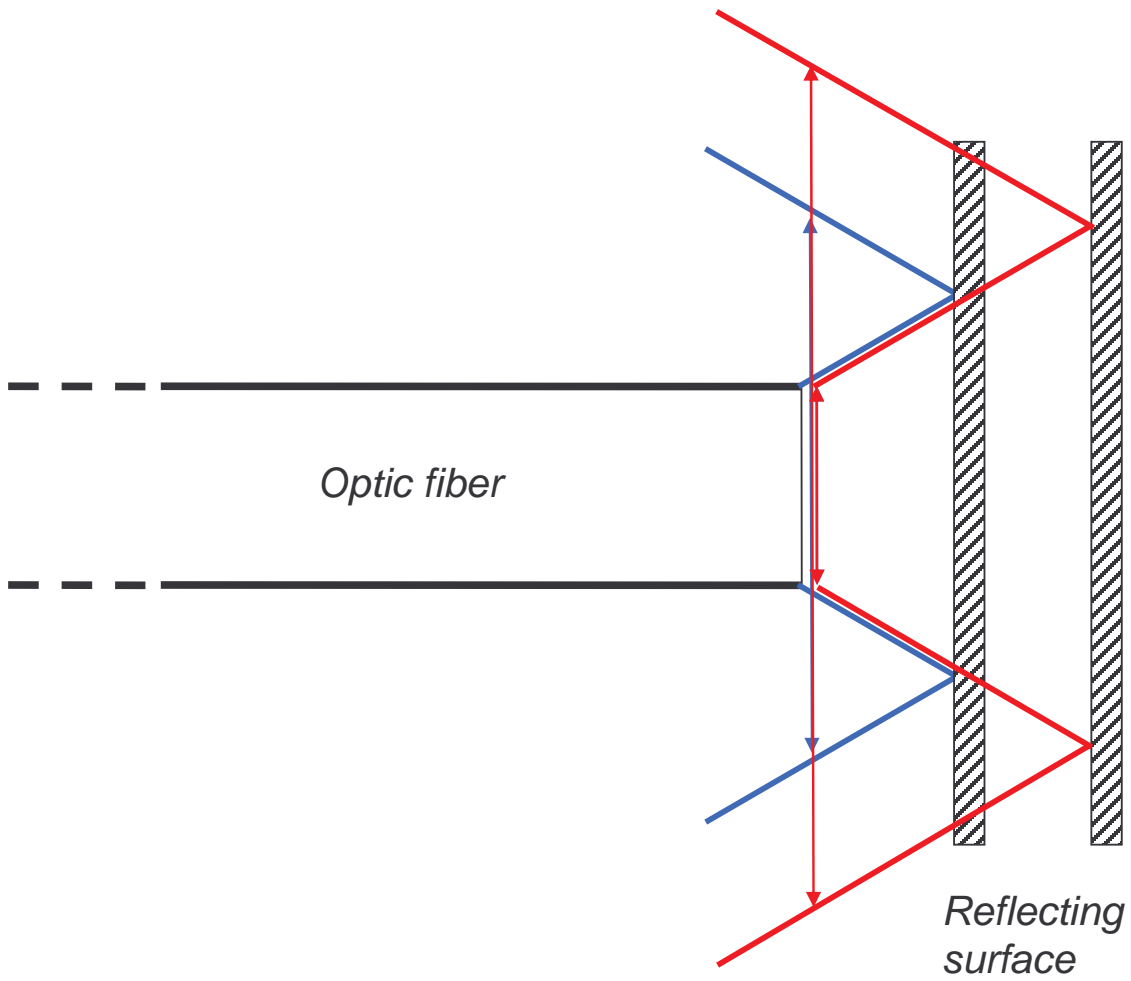
**Figure 2.1:** Optic lever principle: the light exits the optic fiber with an angle, therefore only a portion comes back into the fiber after reflection on a surface. The proportion of reflected light reentering the fiber depends on the distance between the fiber and the reflecting surface.
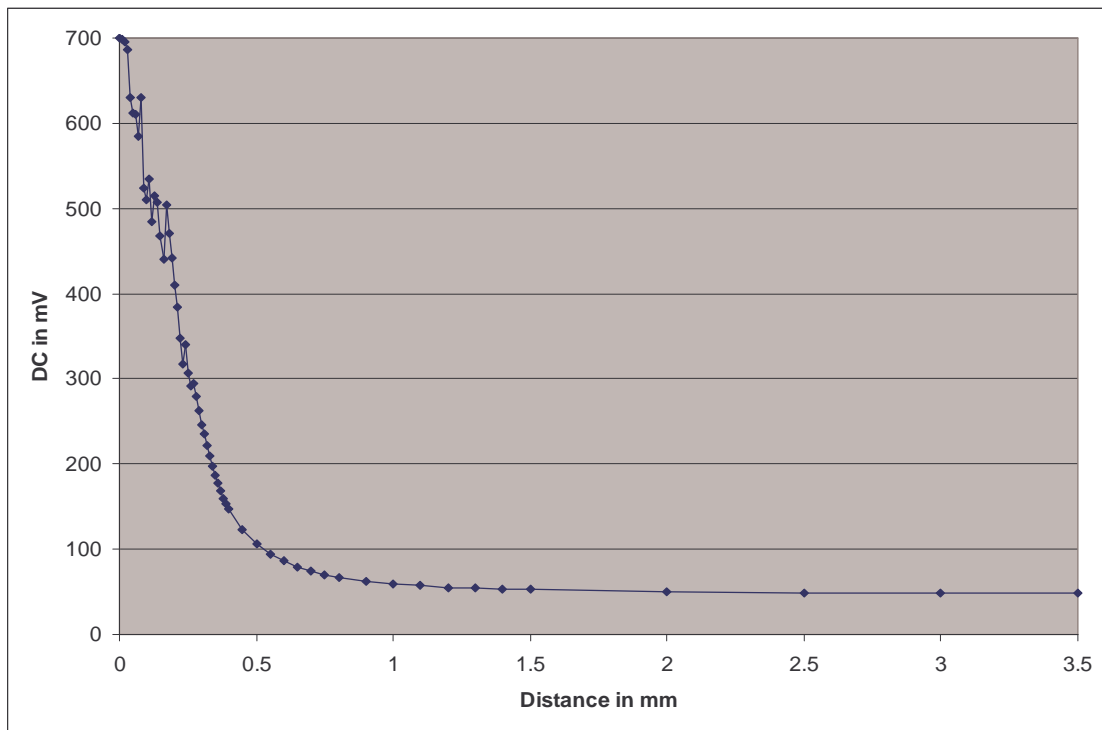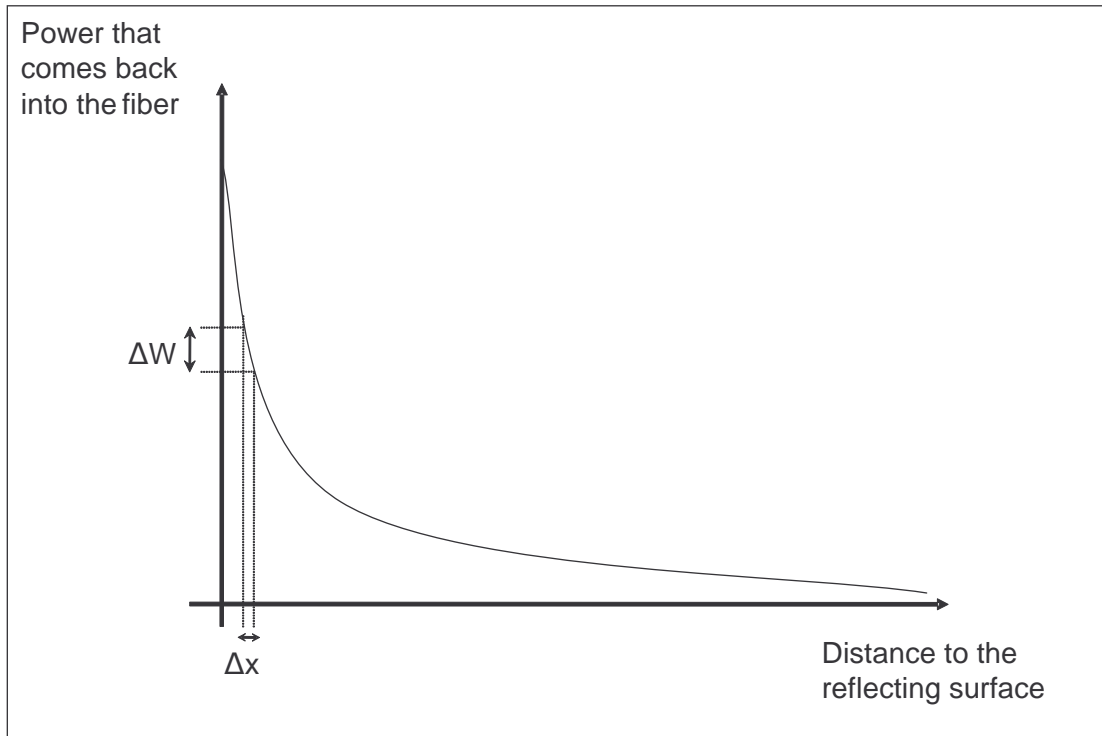
**Figure 2.2:** Reentering power dependence on the distance of the reflecting surface. *Top panel:* theoretical curve (the steepest slopes occur for short distances). *Bottom panel:* empirical curved obtained by monitoring the DC voltage of a photodiode collecting the reentering light reflected by a mirror whose distance from the fiber was varied.
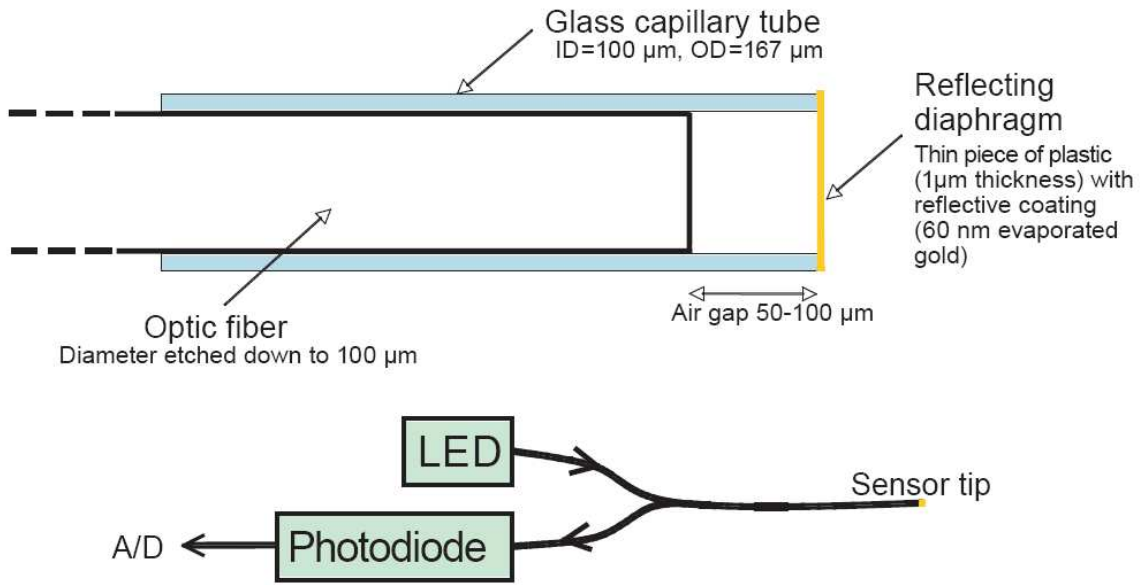
**Figure 2.3:** Schematic of a fiber-optic pressure sensor (after Olson, 1998)
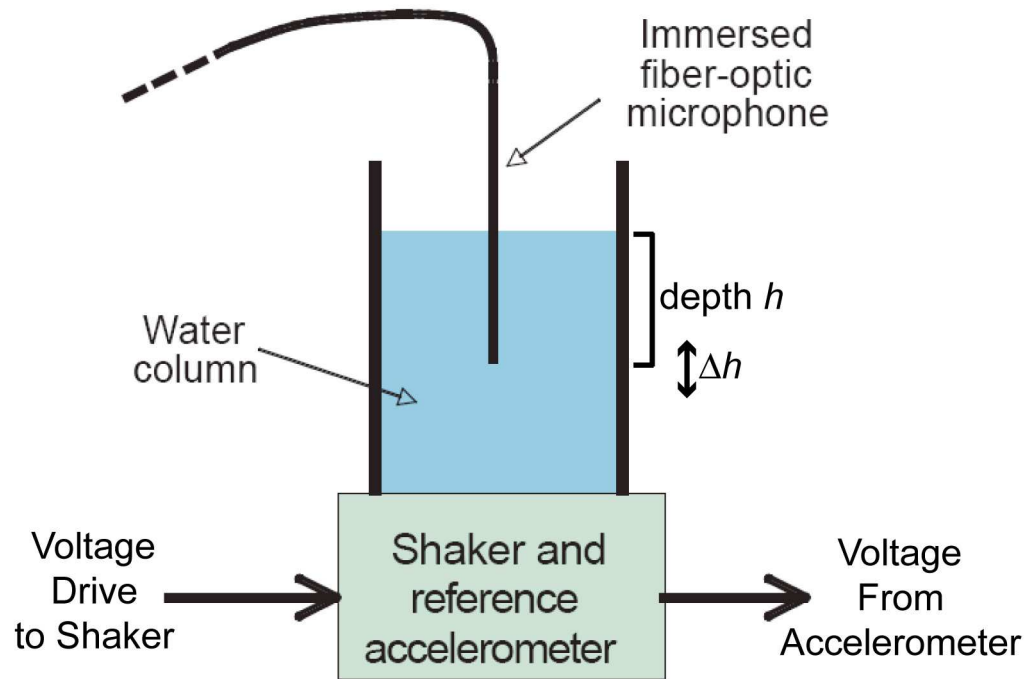
**Figure 2.4:** Fiber-optic pressure sensor calibration in water (after Schloss and Strasberg, 1962). The acceleration provided by the shaker is related to $-\omega^2 \, \Delta h/2$, where $\omega$ is the radian frequency of a sinusoidal stimulus, and $\Delta h$ is the peak-to-peak amplitude of the shaker motion.
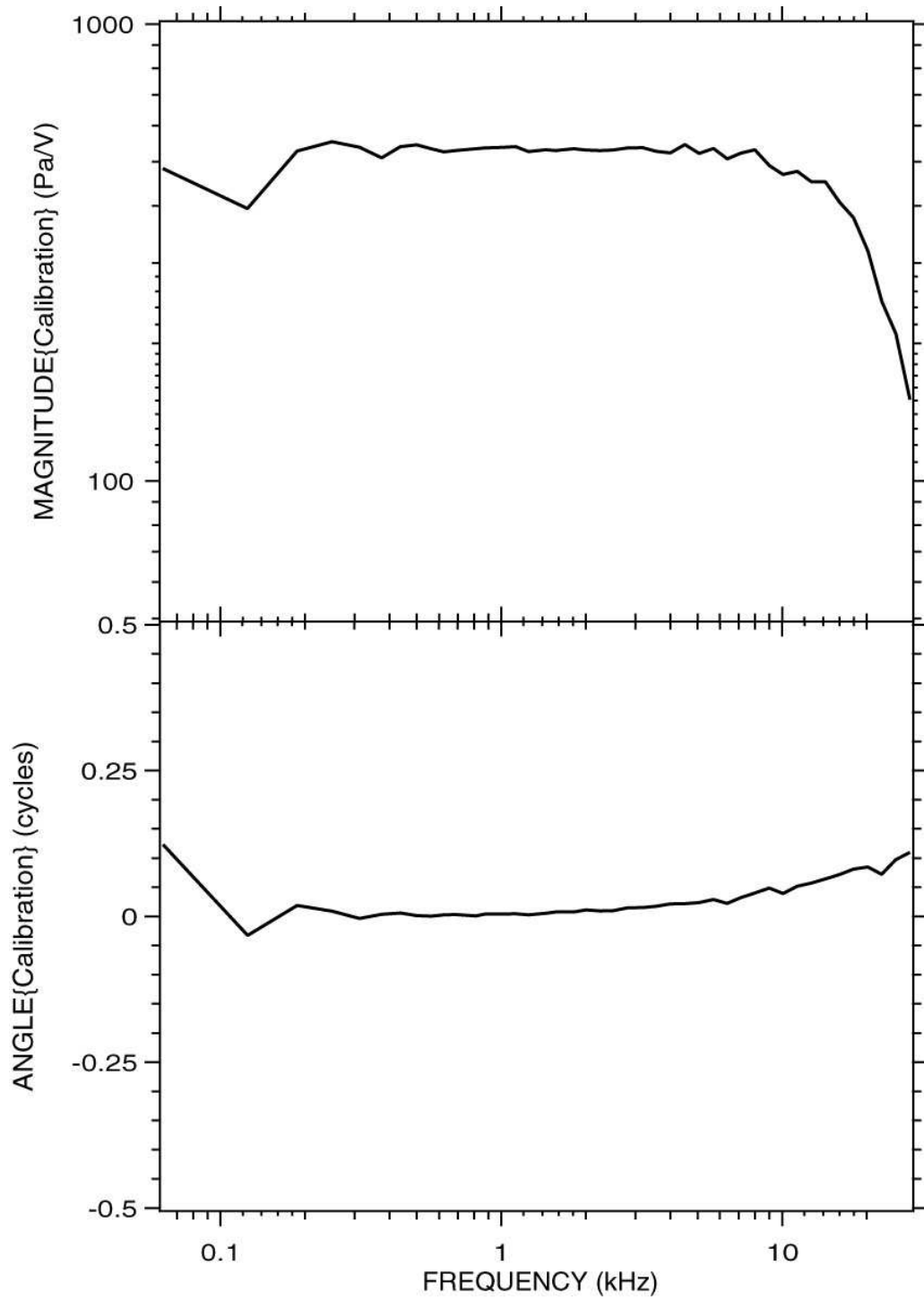
**Figure 2.5:** Example of water calibration function (pressure sensor #44 on 07/26/07)
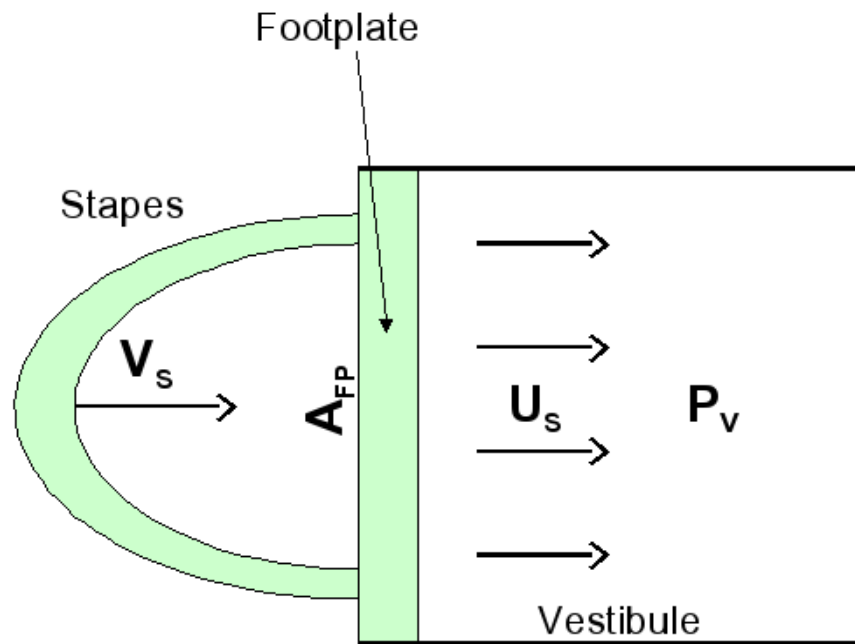
**Figure 2.6:** Stapes volume velocity as the product of linear velocity by footpkate area (piston-like motion hypothesis).
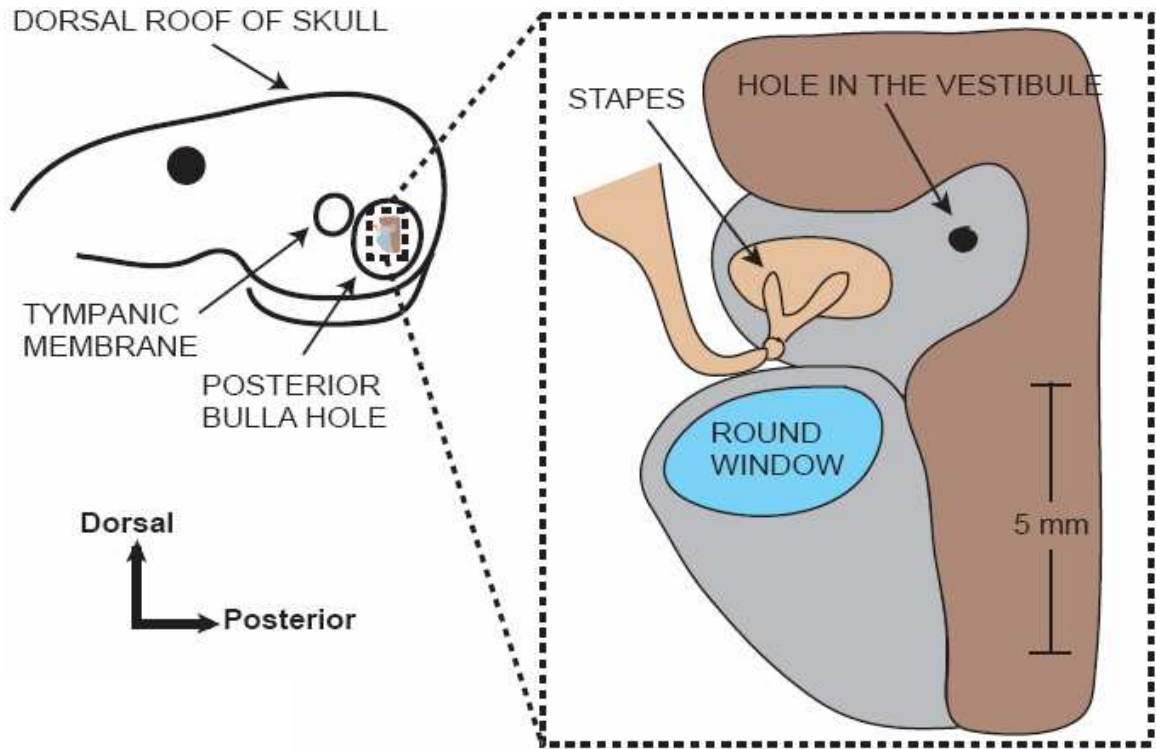
**Figure 2.7:** Placement of the hole in the vestibule.
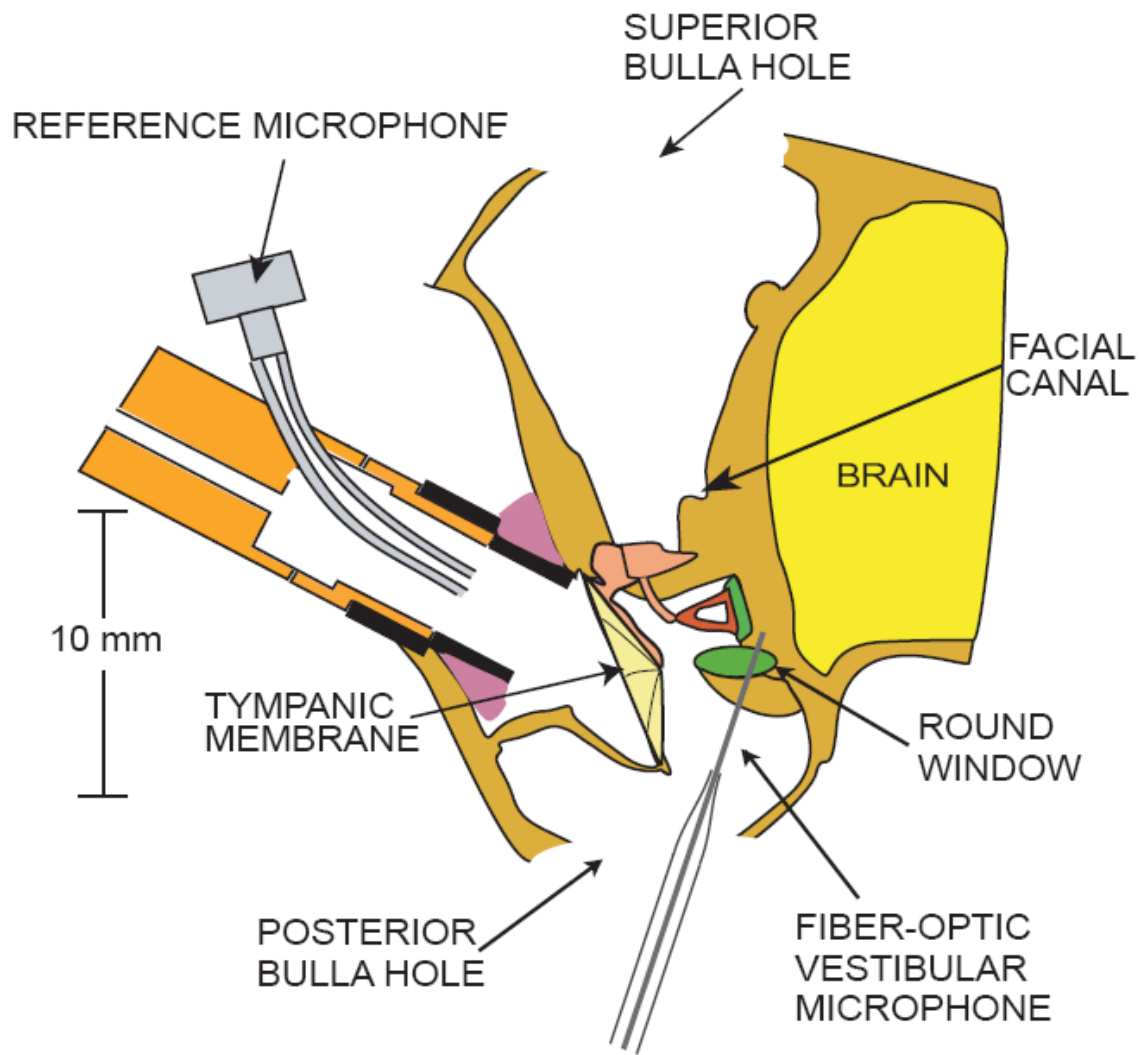
**Figure 2.8:** Sound-source and reference microphone in the ear canal and placement of the fiber-optic pressure sensor in the vestibule.
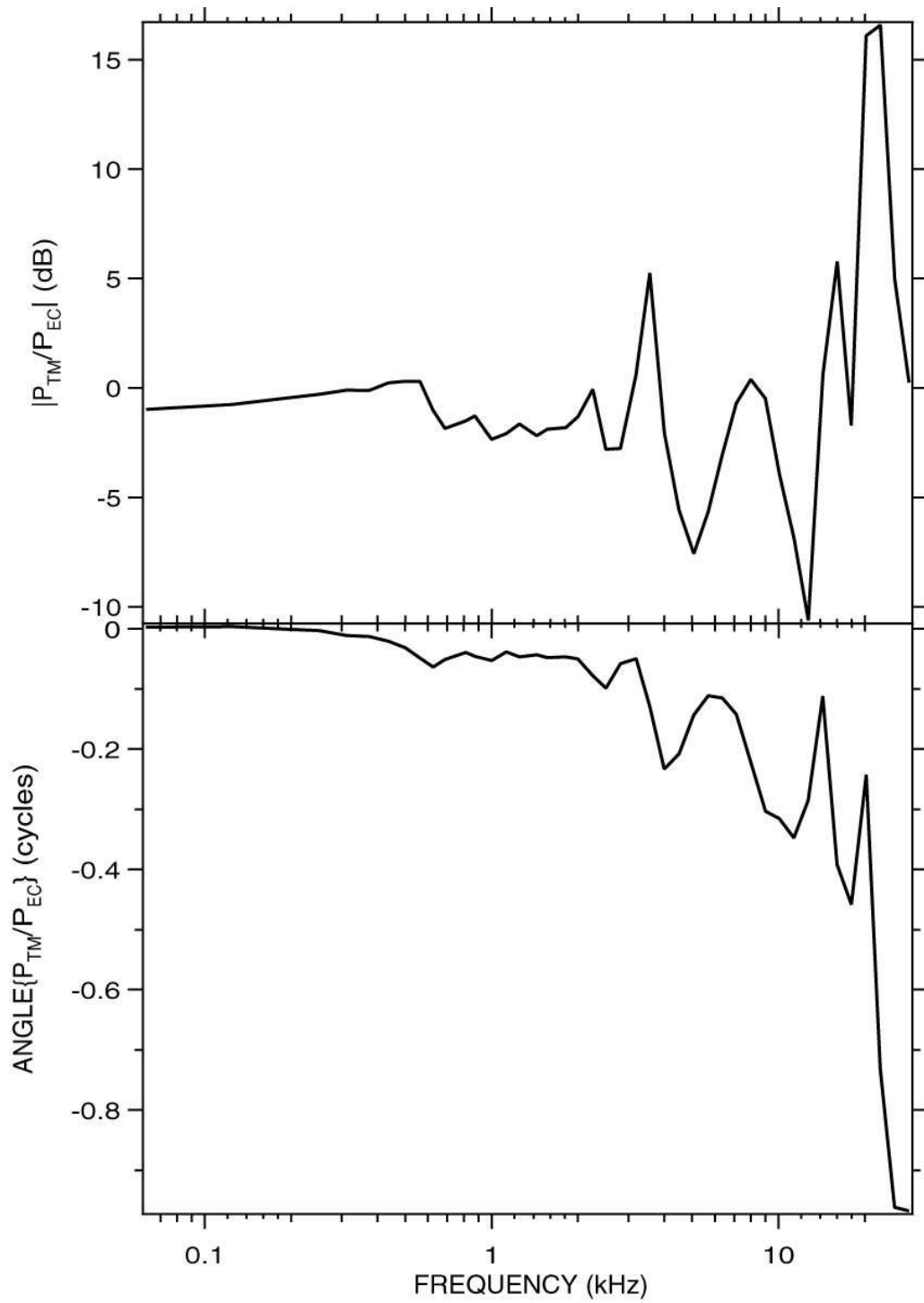
**Figure 2.9:** Transfer function between the sound pressure in the ear canal about 10 mm from the TM $P_{EC}$, and close to the TM $P_{TM}$, measured in a dead ear.
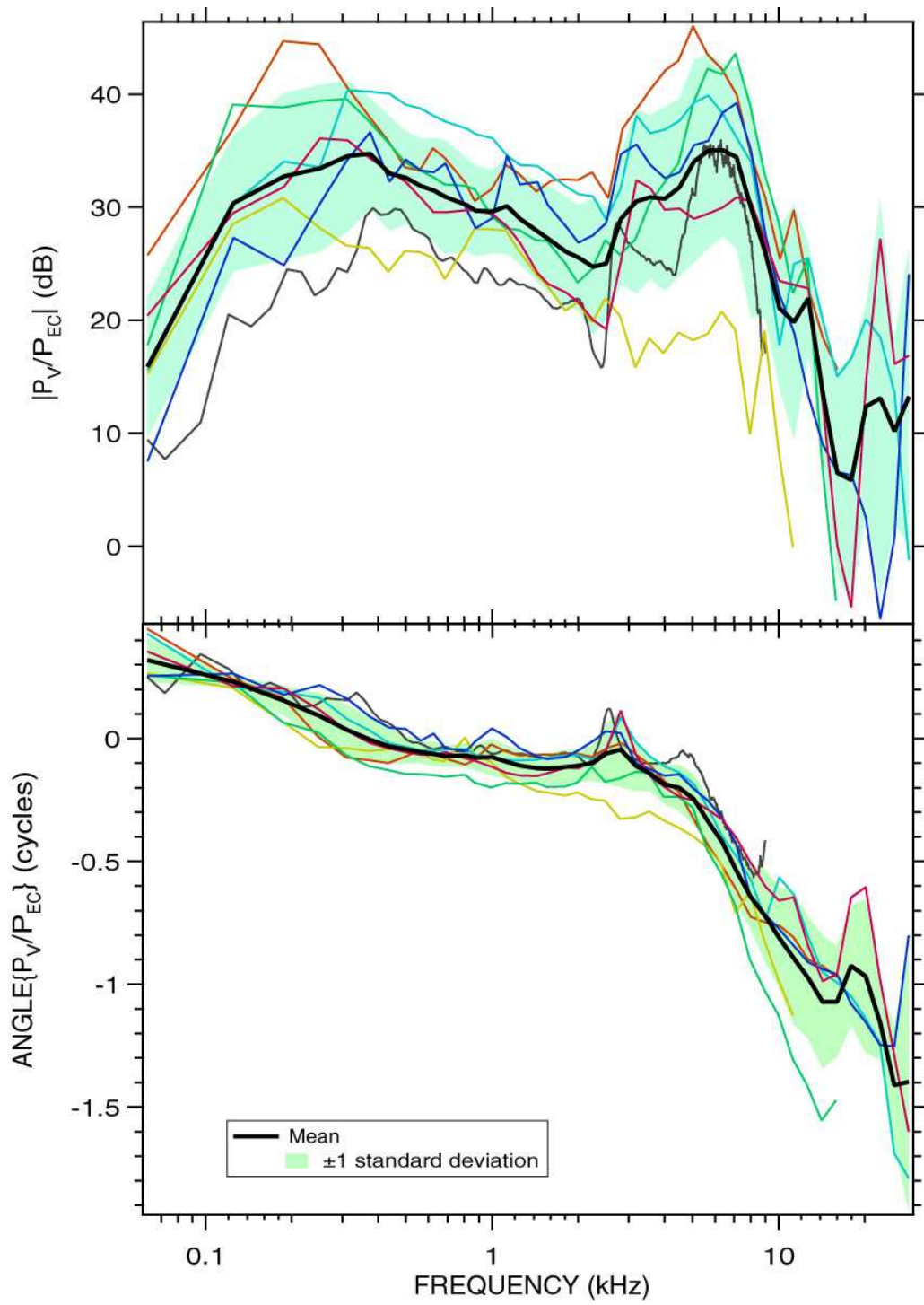
**Figure 3.1:** Measured middle ear gain $P_V/P_{EC}$ in 7 animals.
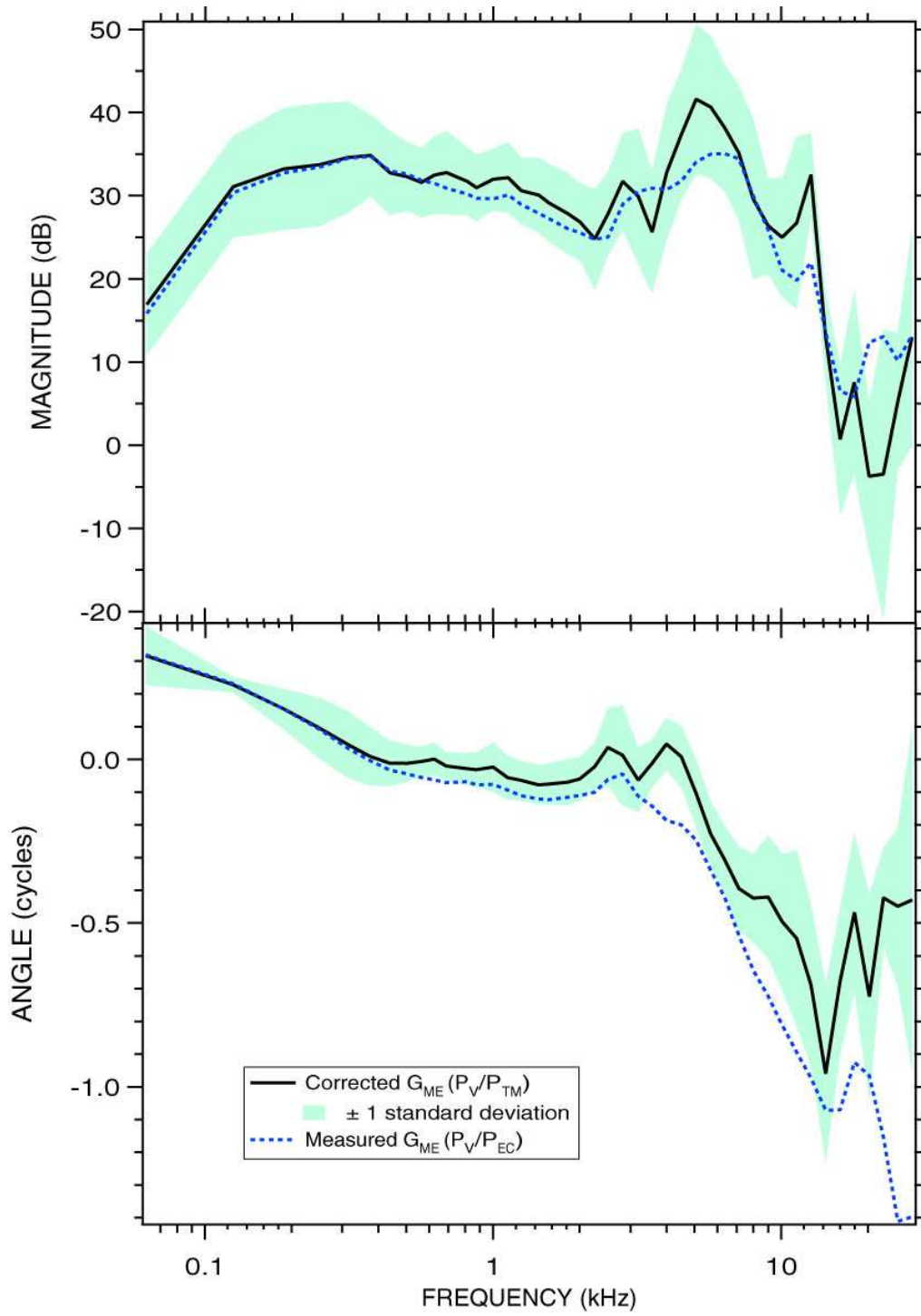
**Figure 3.2:** Corrected middle ear gain $P_V/P_{TM}$.
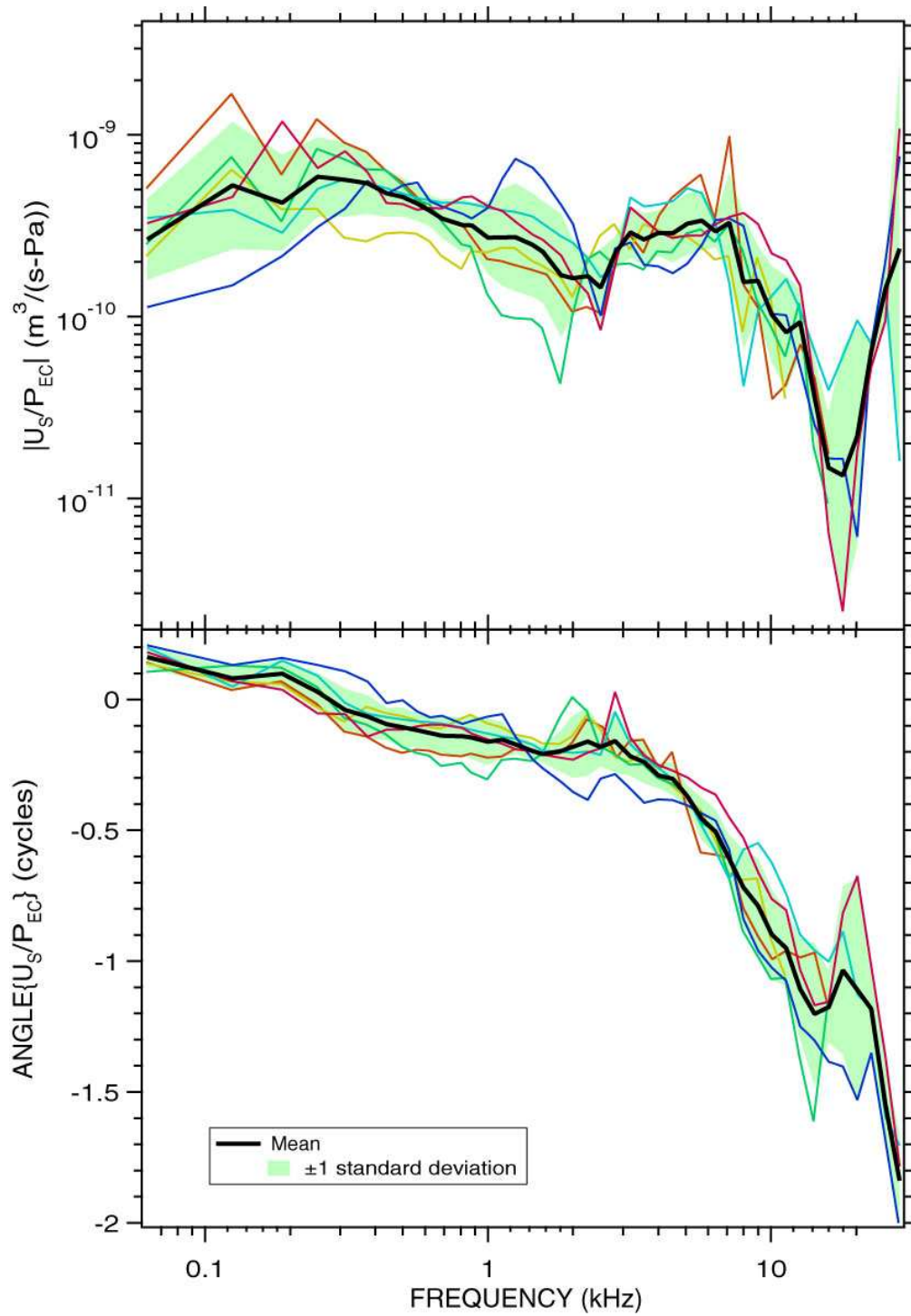
**Figure 3.3:** Measured normalized stapes volume velocity $U_S/P_{EC}$ in 6 animals (intact vestibule).
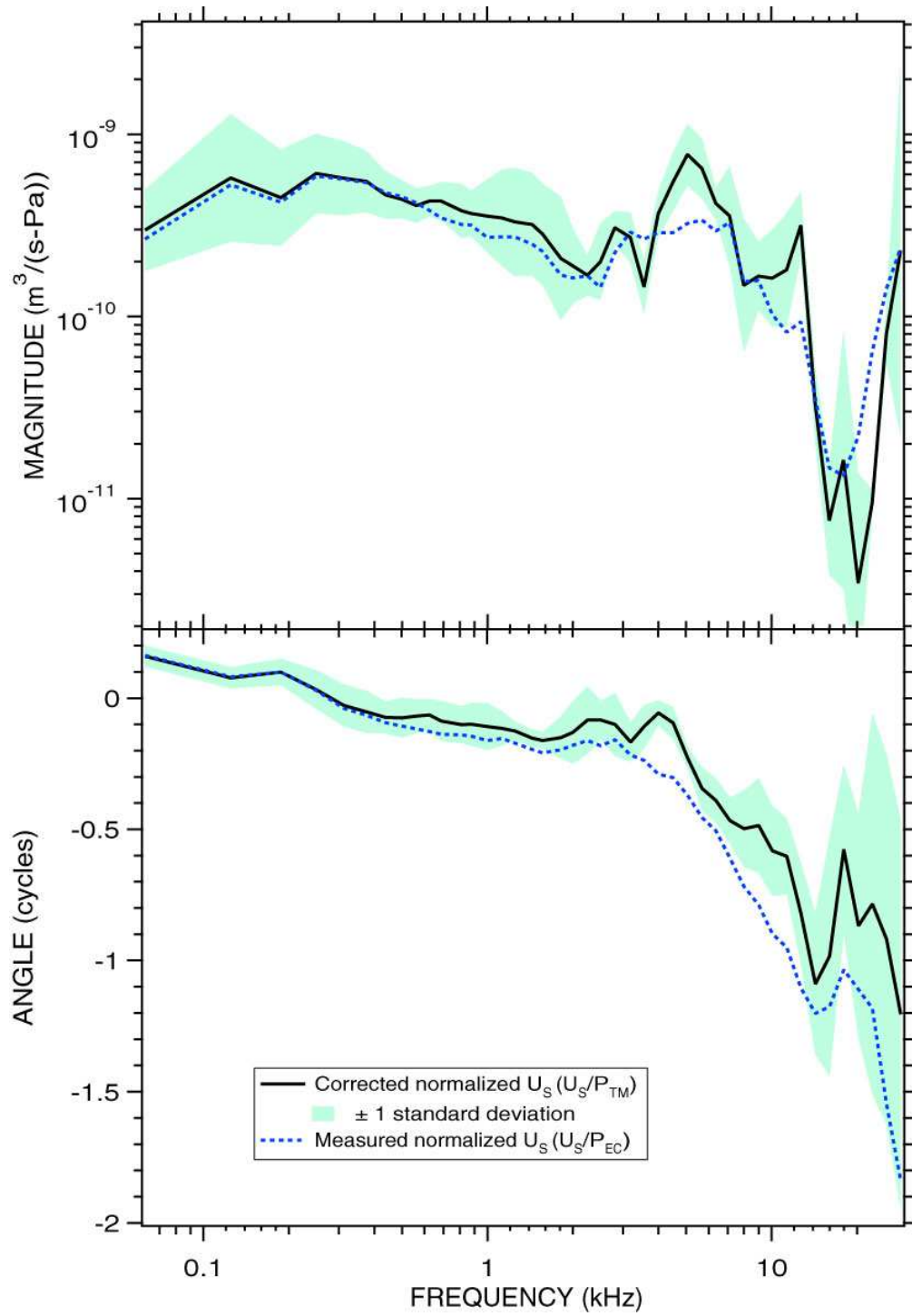
**Figure 3.4:** Corrected normalized stapes volume velocity $U_S/P_{TM}$ in 6 animals (intact vestibule).
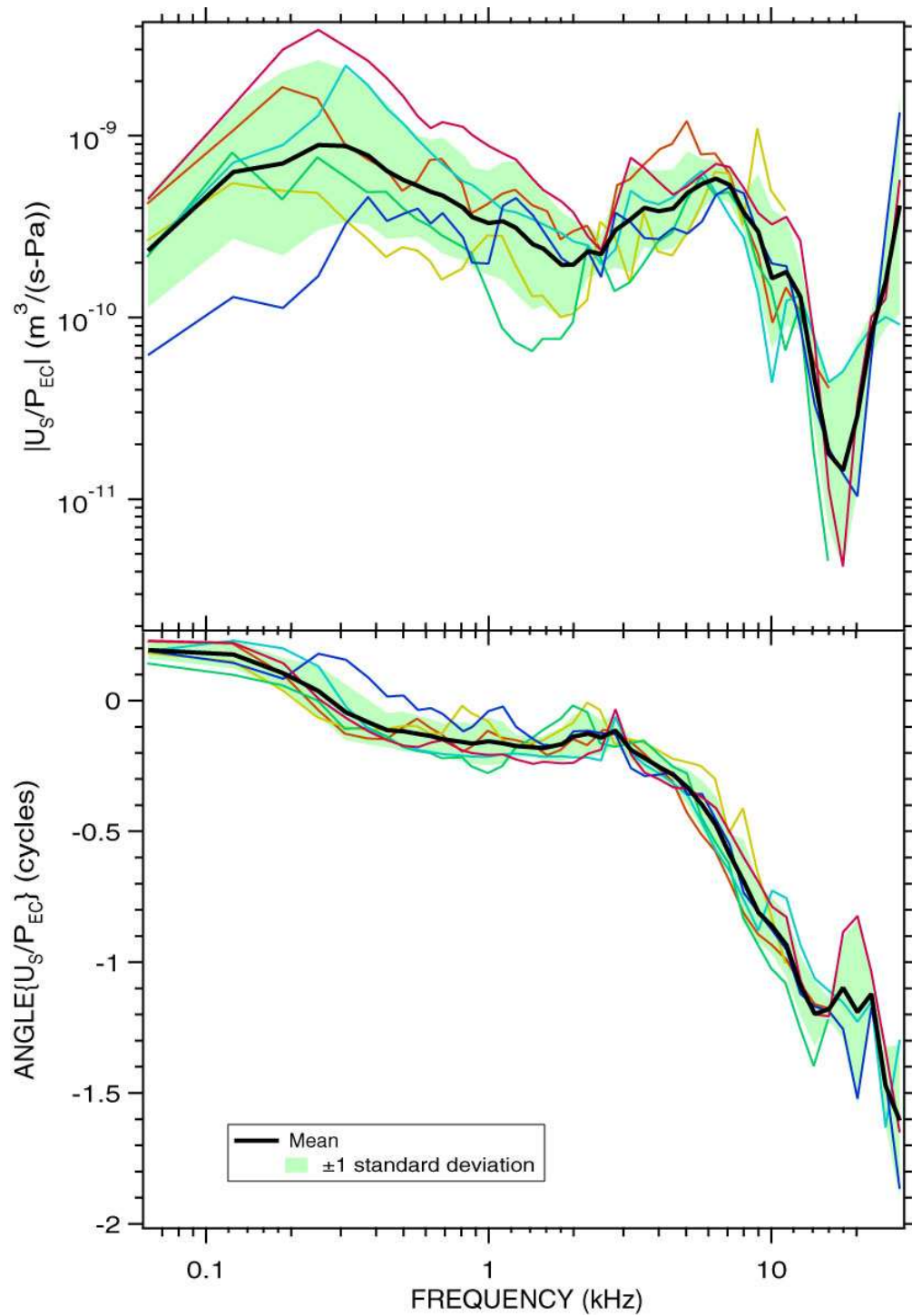
**Figure 3.5:** Normalized stapes volume velocity $U_S/P_{EC}$ in 6 animals, with a ≈250 μm hole in the vestibule and the pressure sensor in place.
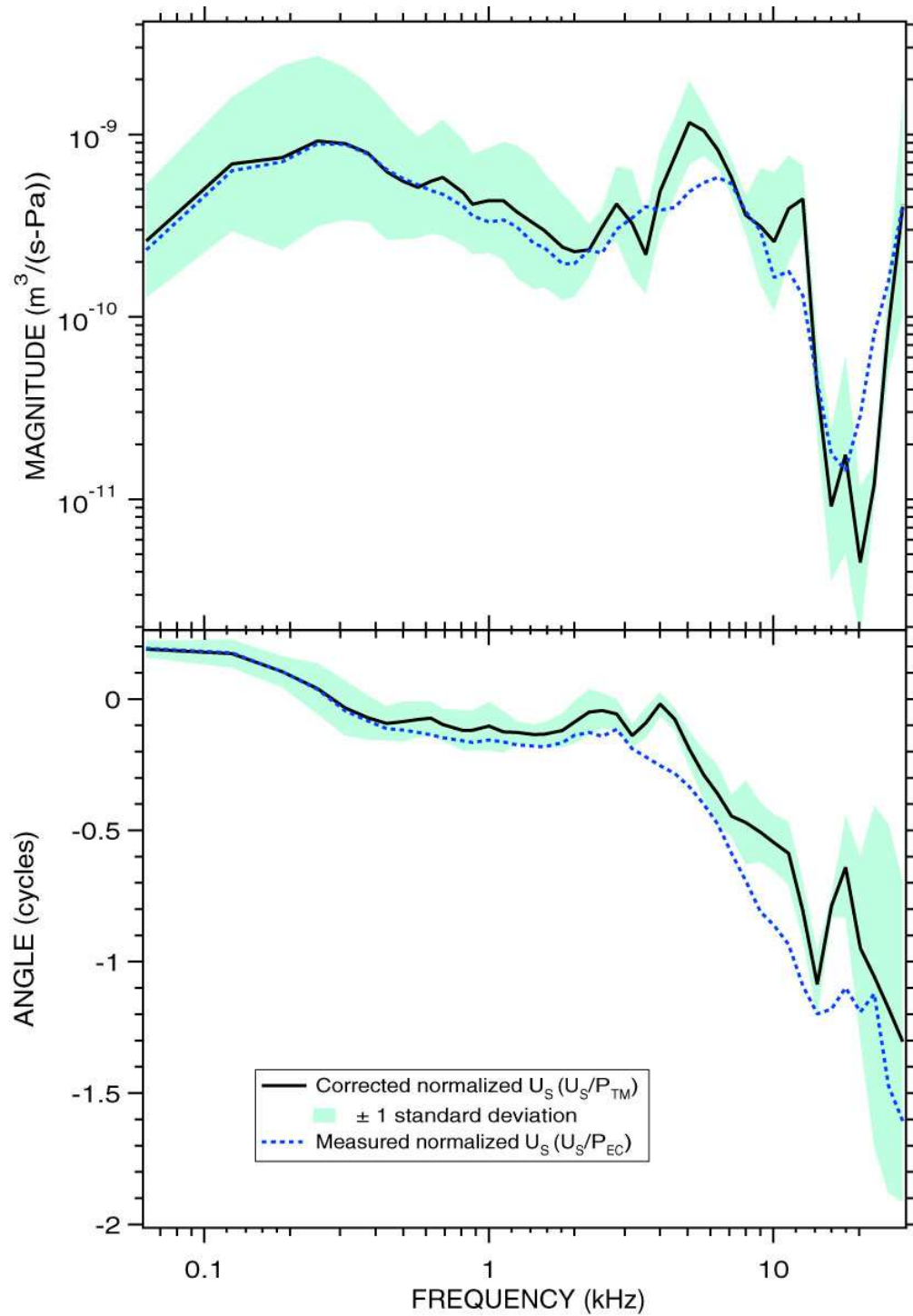
**Figure 3.6:** Corrected normalized stapes volume velocity $U_S/P_{TM}$ in 6 animals, with a $\approx 250$ μm hole in the vestibule and the pressure sensor in place.
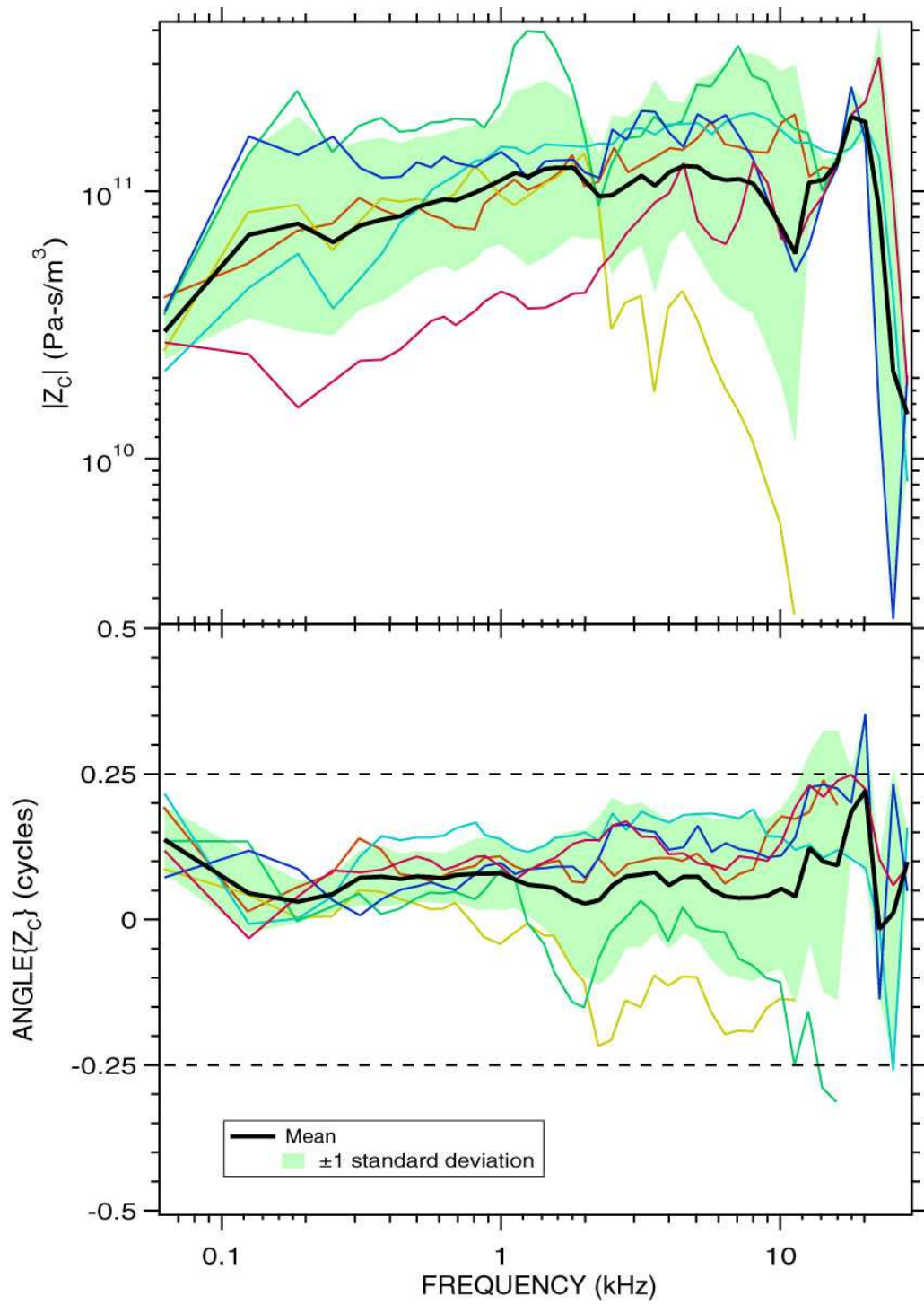
**Figure 3.7:** Cochlear input impedance $Z_C$ in 6 animals.
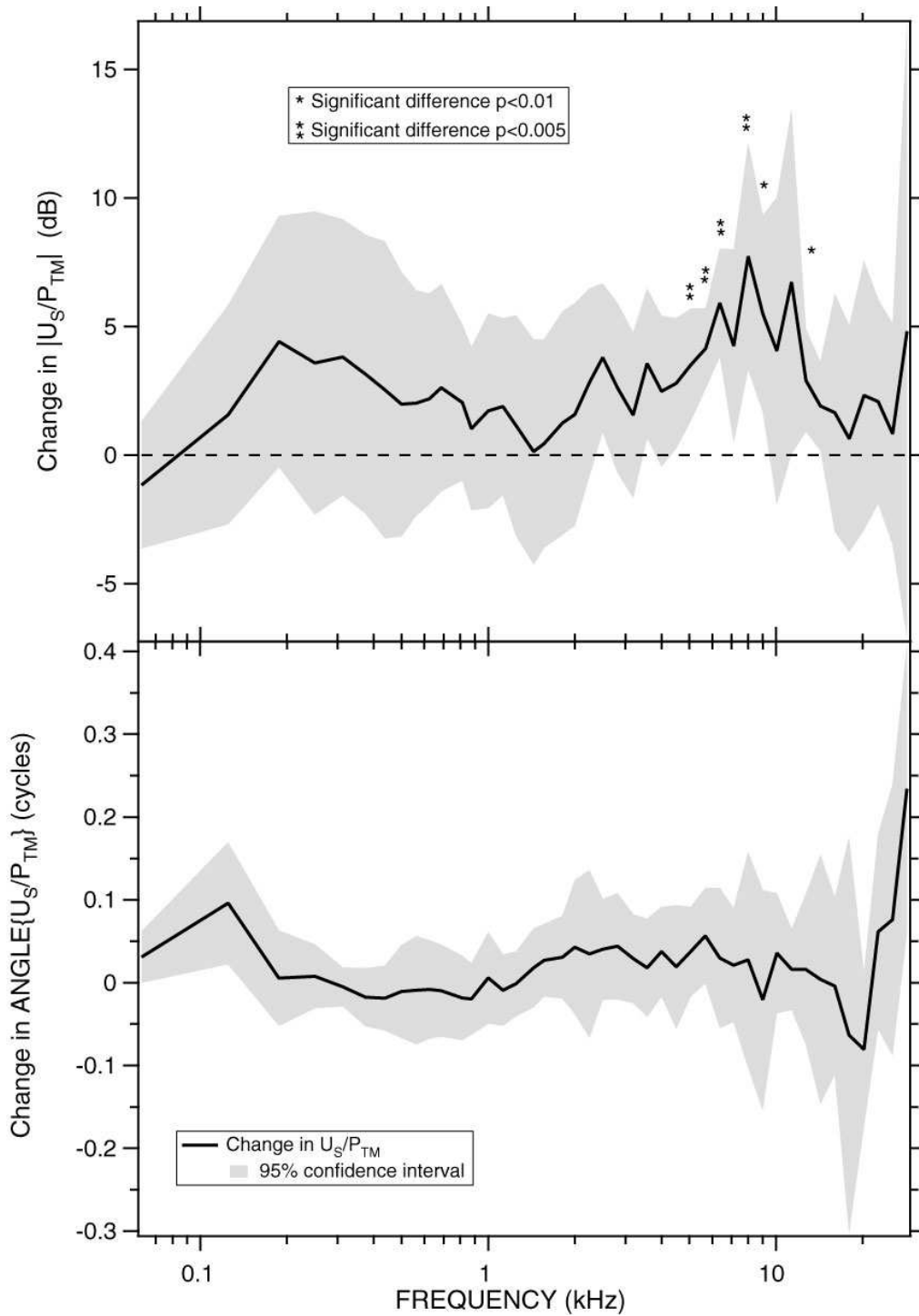
**Figure 4.1:** Influence of the vestibular hole on $U_S/P_{TM}$ in 6 animals. For each animal, $U_S/P_{TM}$ measured with the hole and pressure sensor in place was divided by $U_S/P_{TM}$ measured with an intact vestibule. The average of these ratios, plotted here with the 95% confidence interval, represents the change due to the introduction of the hole.
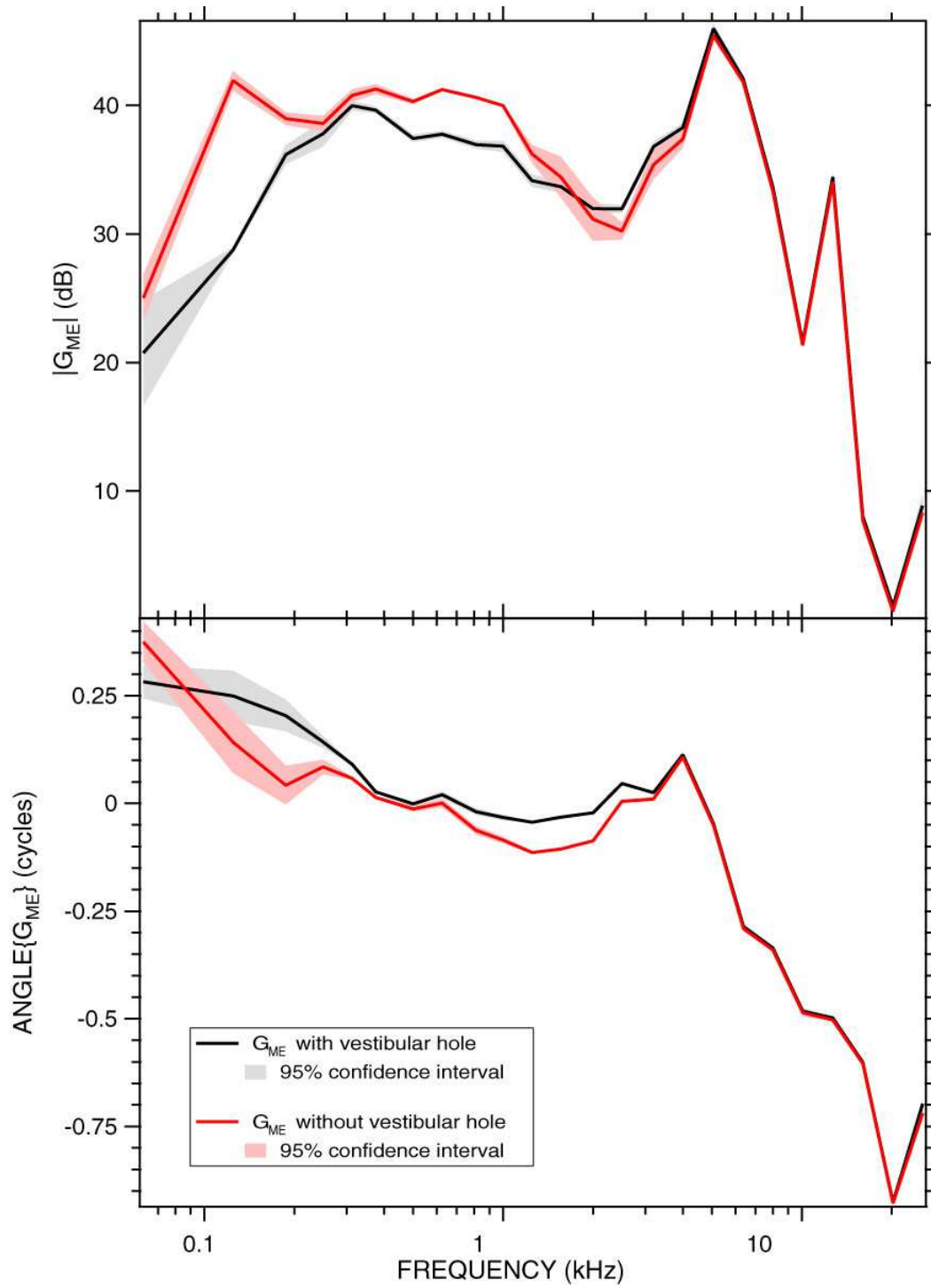
**Figure 4.2:** Influence of the vestibular hole on $G_{ME}$ in 1 animal. Vestibular pressure went up at low frequencies after plugging the hole with a very viscous gel, and went back to the lower level after removing the gel.
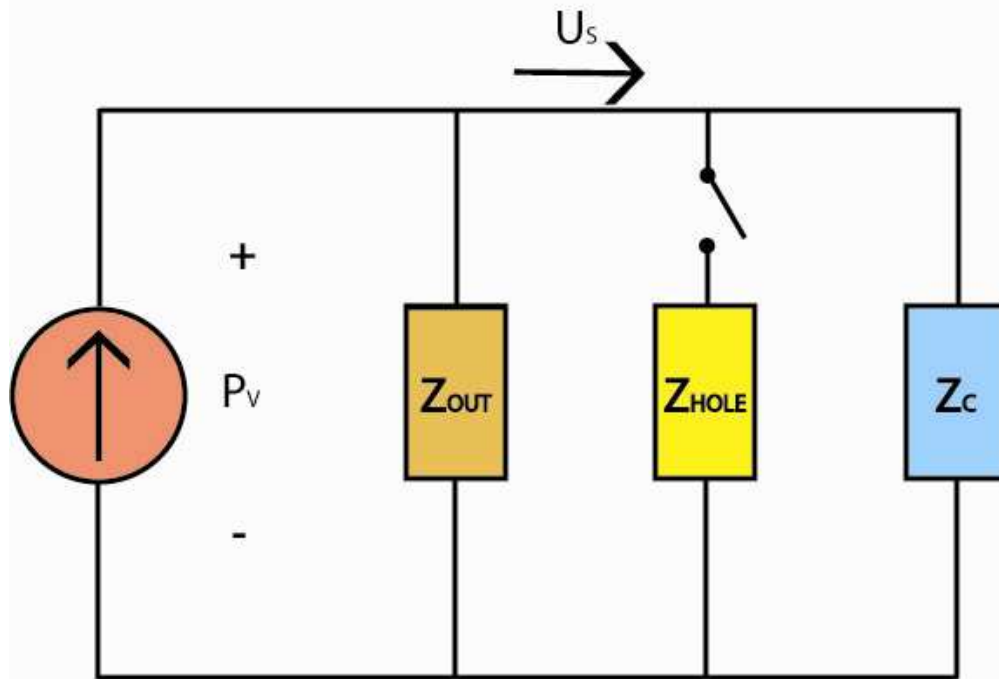
**Figure 4.3:** Lumped-element model of the middle and inner ears with or without a vestibular hole. $Z_{OUT}$ is the output impedance of the middle ear, $Z_{HOLE}$ the impedance of the hole, and $Z_C$ the input impedance of the cochlea.
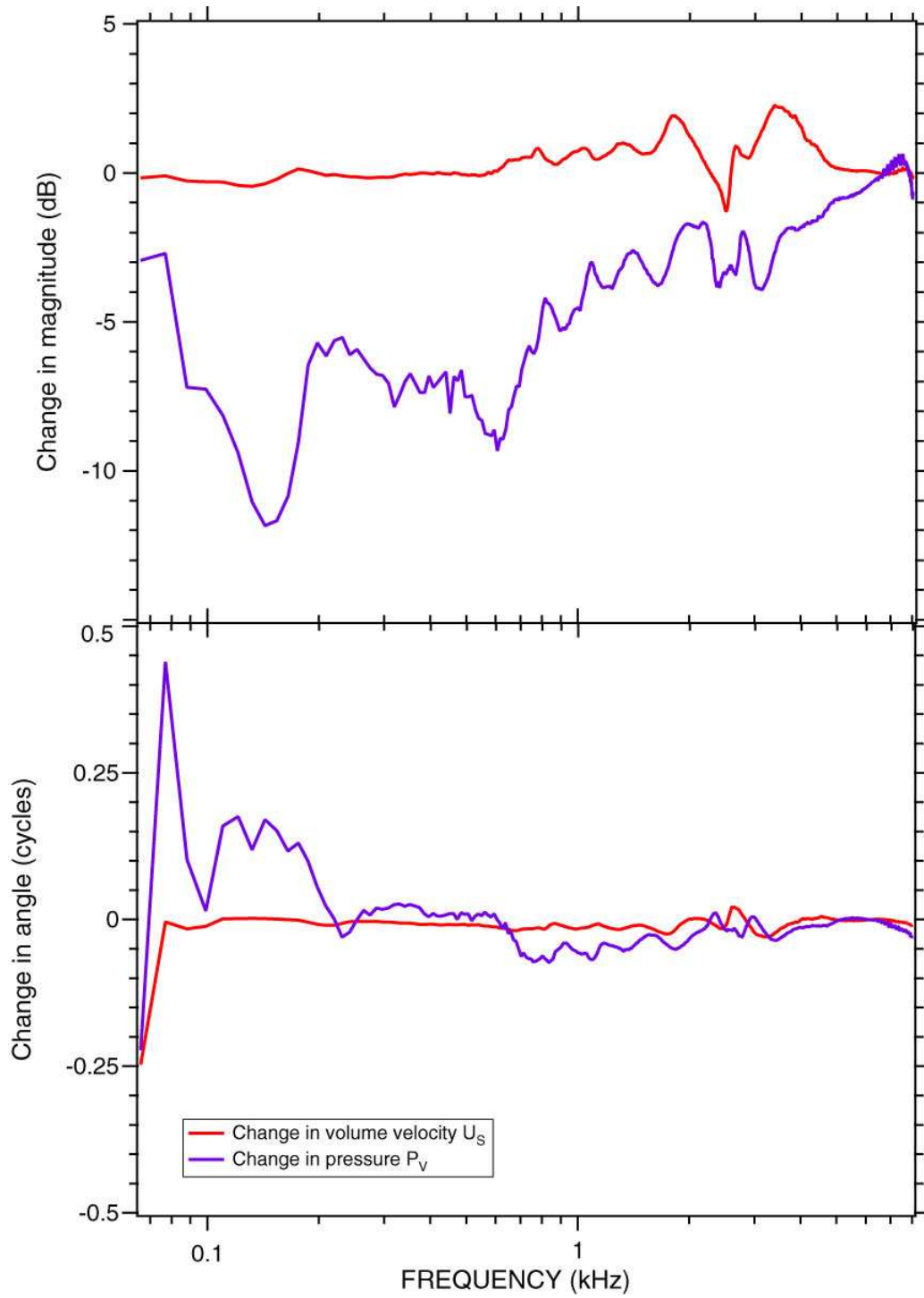
**Figure 4.4:** Changes in $U_S$ and $P_V$ after introduction of 200 μm hole partially filled with the pressure sensor, as predicted by the model in Figure 4.3
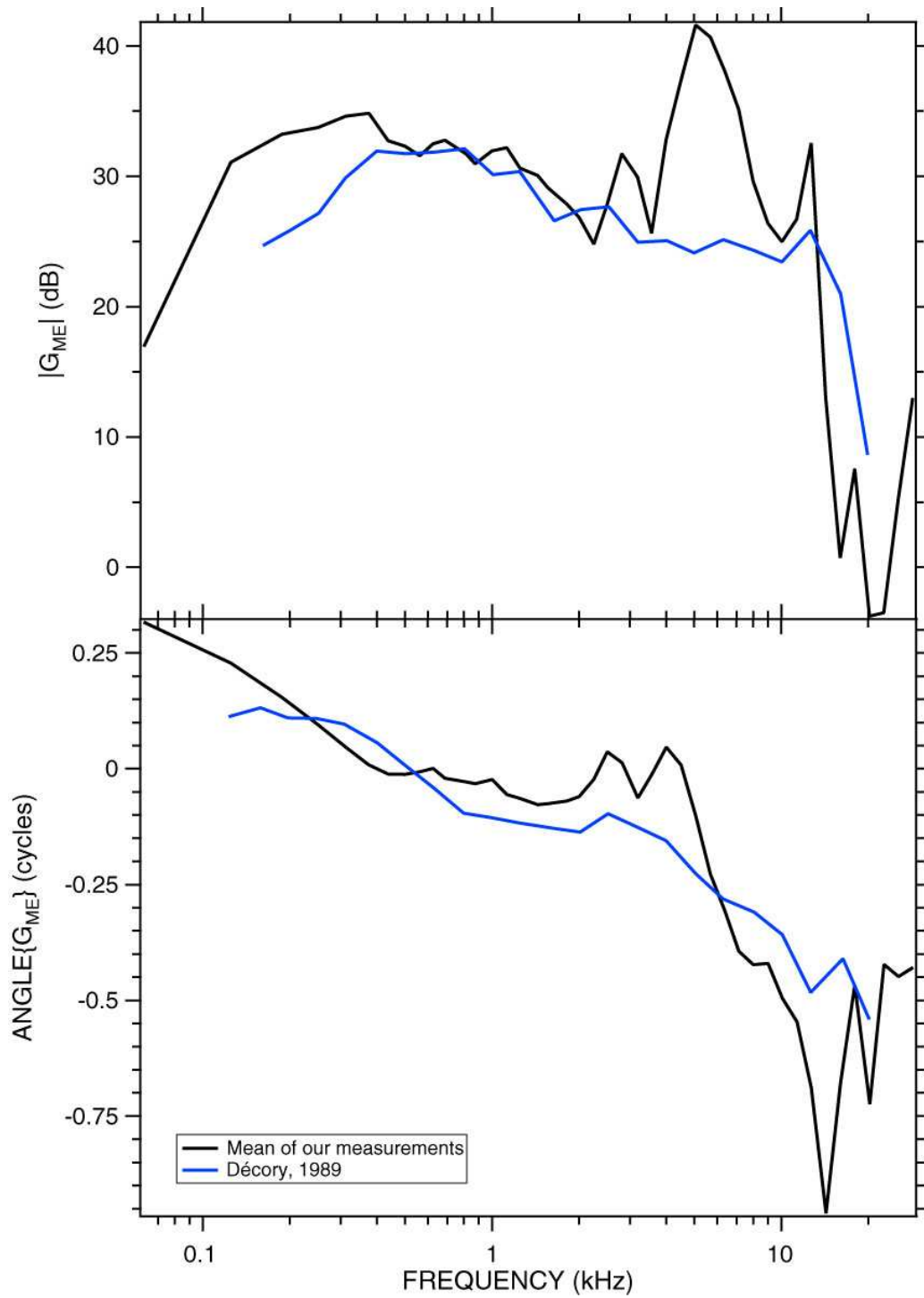
**Figure 4.5:** Comparison of our measurements of middle ear gain $G_{ME} = P_V/P_{TM}$ with another study in the chinchilla (Décory, 1989)
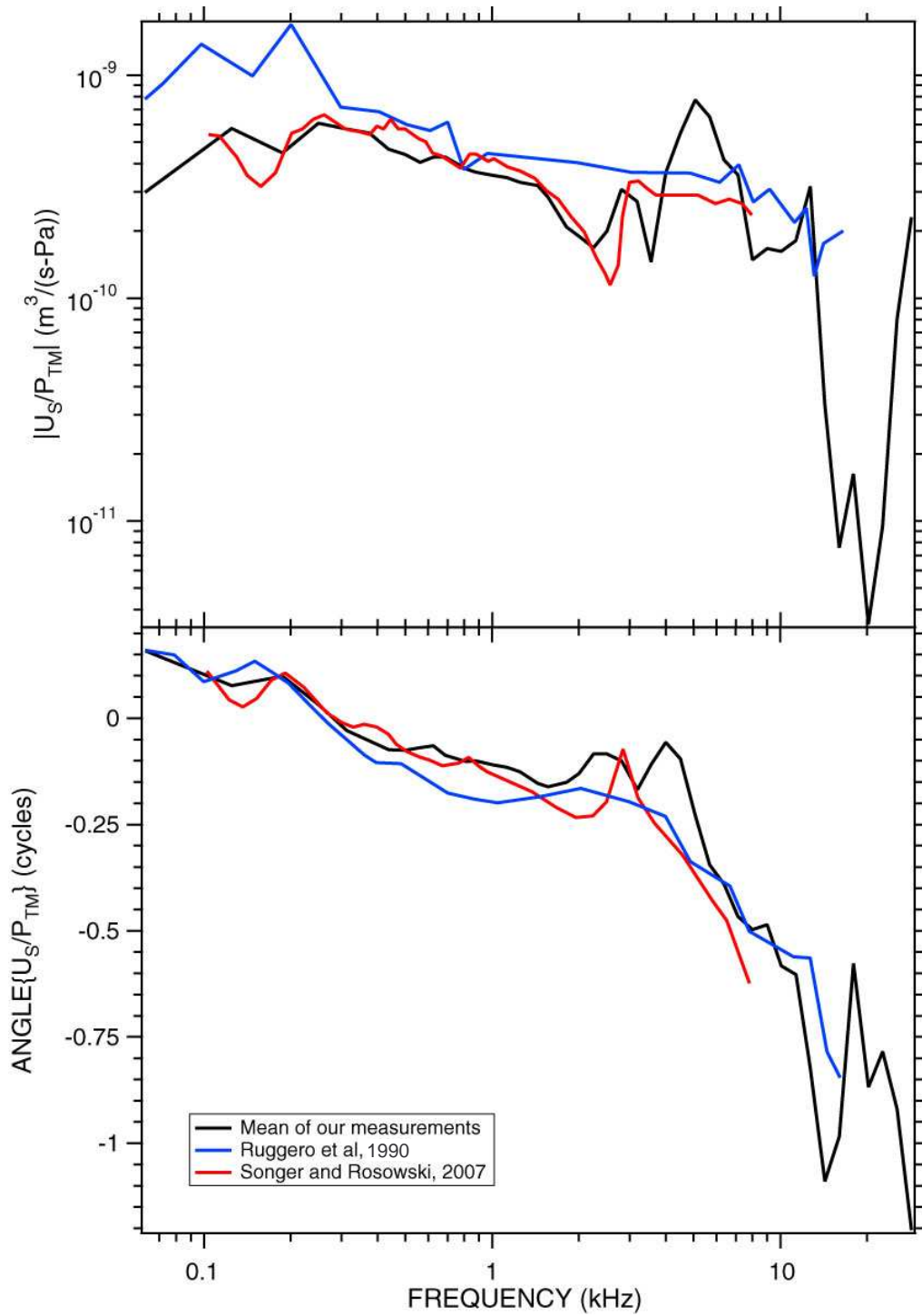
**Figure 4.6:** Comparison of our $U_S/P_{TM}$ with other chinchilla studies (Songer and Rosowski, 2007a and Ruggero *et al.*, 1990)
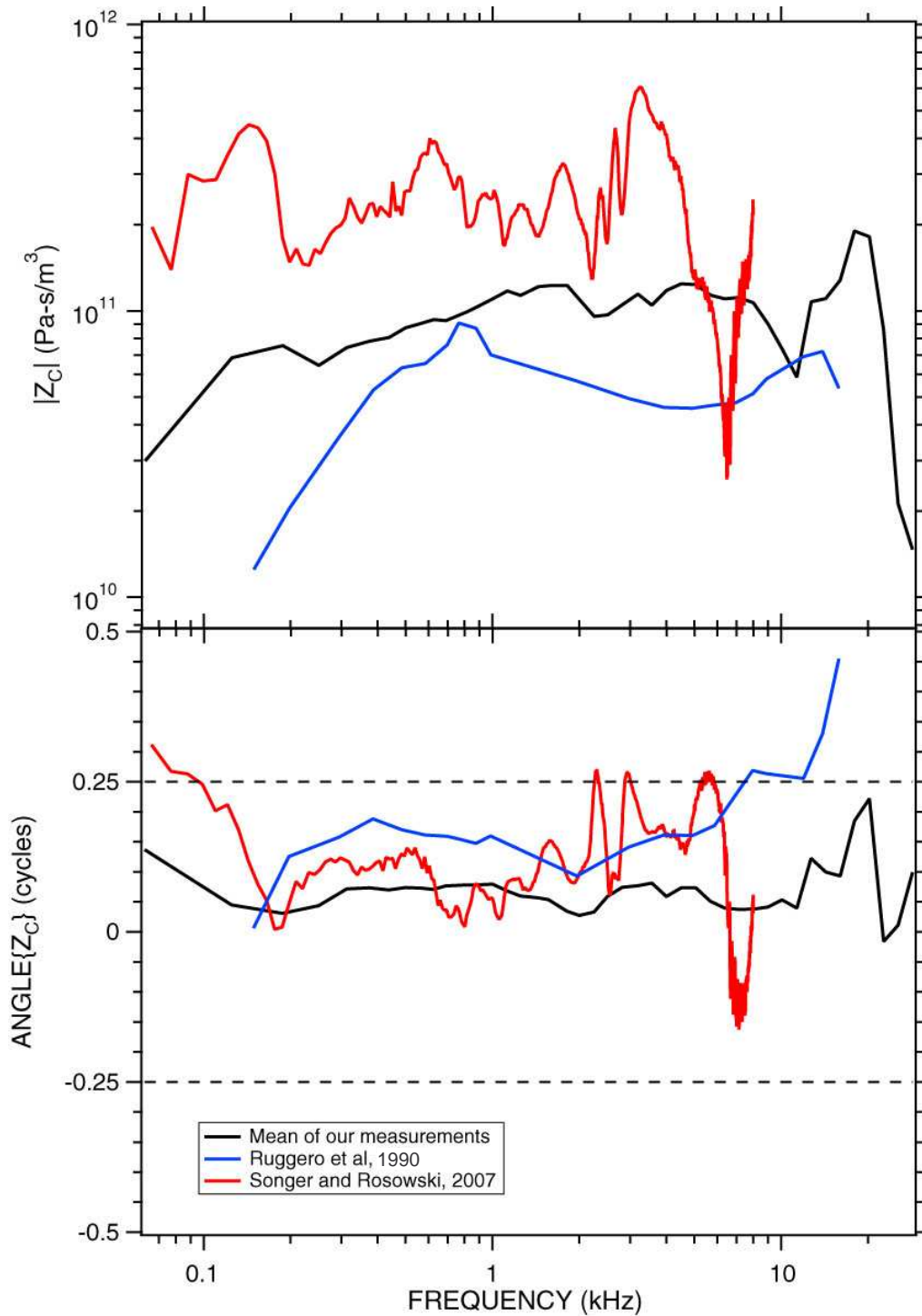
**Figure 4.7:** Comparison of our measurements of $Z_C$ with two other chinchilla studies: a model by Songer and Rosowski (2007a) and computations by Ruggero *et al.* (1990), who used their own $U_S$ measurements and Décory's $P_V$ measurements in different ears.
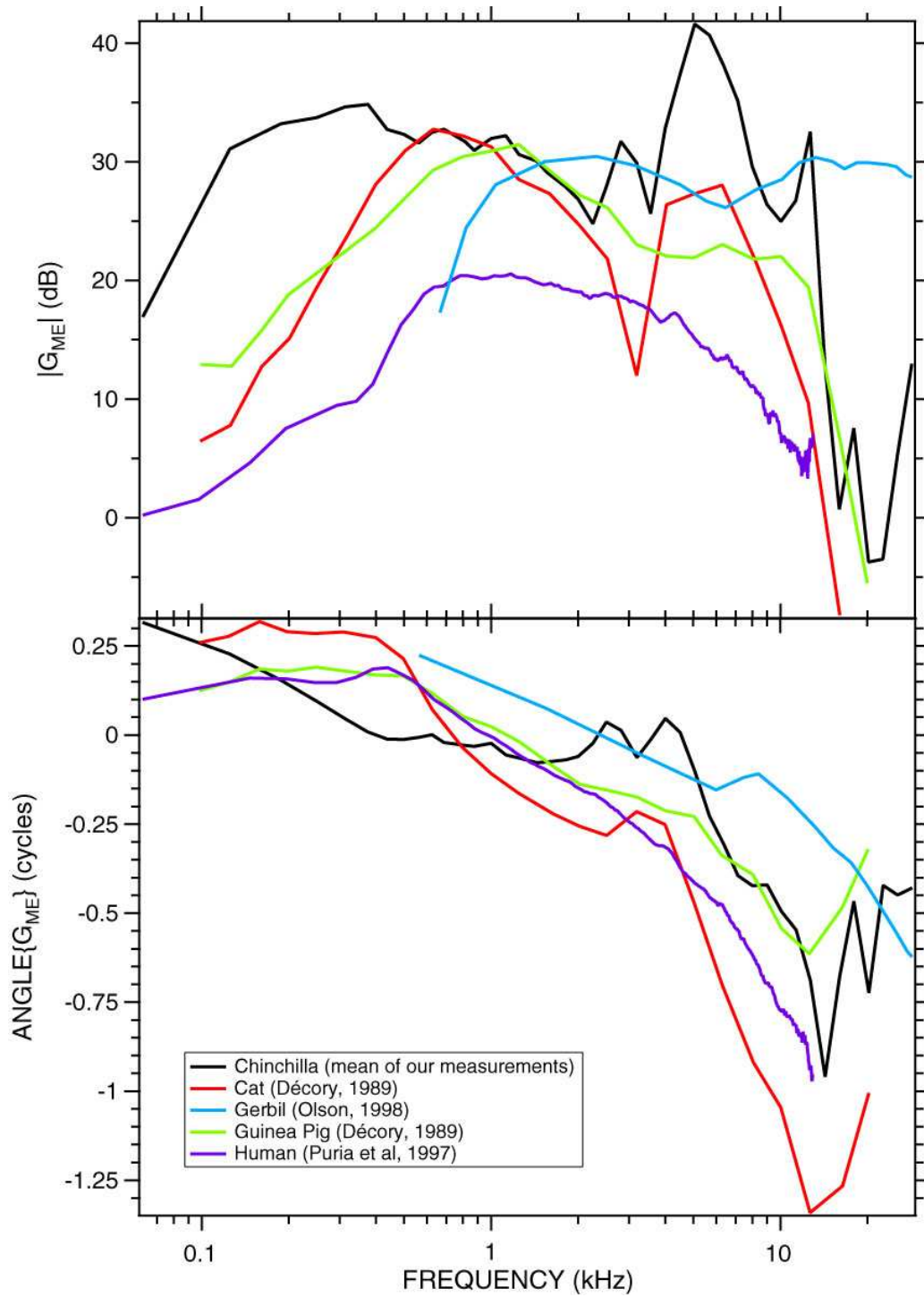
**Figure 4.8:** Comparison of our measurements of $G_{ME}$ with measurements in other species: data from cat, guinea pig (Décory, 1989), gerbil (Olson, 1998) and human temporal bone (Puria *et al*., 1997)
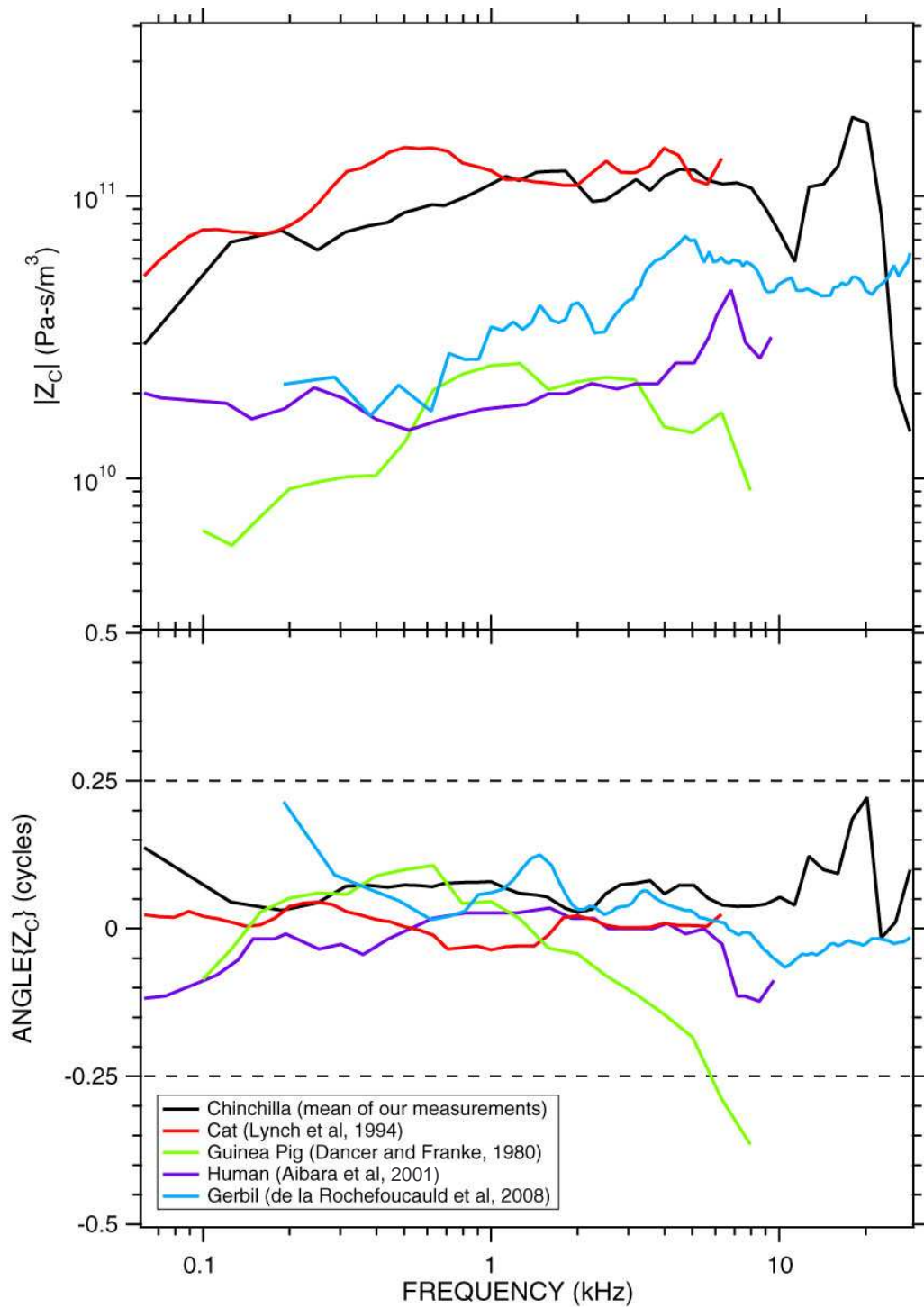
**Figure 4.9:** Comparison of our measurements of $Z_C$ with measurements in other species: data from cat (Lynch *et al.*, 1994), guinea pig (Dancer and Franke, 1980), gerbil (de la Rochefoucauld *et al.*, 2008) and human temporal bone (Aibara *et al.*, 2001)
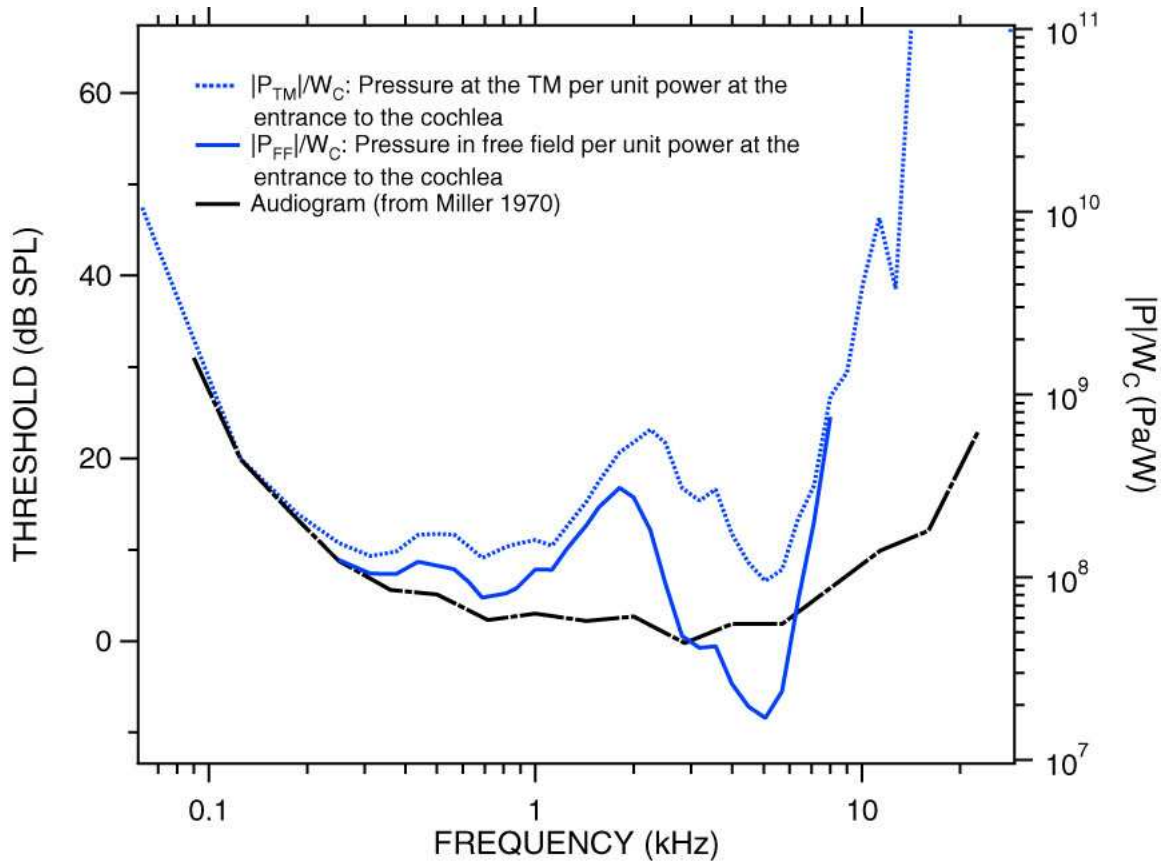
**Figure 4.10:** Comparison of an average chinchilla audiogram (from Miller, 1970) with our average $|P_{TM}|/W_C$ and $|P_{FF}|/W_C$. The free field pressure $P_{FF}$ was obtained from $P_{TM}$ based on an average chinchilla Head Related Transfer Function (HRTF) measured between 250 Hz and 8 kHz by von Bismark and Pfeiffer (1967).